

Star formation and mass assembly in high redshift galaxies

P. Santini^{1,2}, A. Fontana¹, A. Grazian¹, S. Salimbeni^{1,3}, F. Fiore¹, F. Fontanot⁴, K. Boutsia¹, M. Castellano^{1,2}, S. Cristiani⁵, C. De Santis^{6,7}, S. Gallozzi¹, E. Giallongo¹, N. Menci¹, M. Nonino⁵, D. Paris¹, L. Pentericci¹, and E. Vanzella⁵

¹ INAF - Osservatorio Astronomico di Roma, Via Frascati 33, 00040 Monteporzio (RM), Italy

² Dipartimento di Fisica, Università di Roma “La Sapienza”, P.le A. Moro 2, 00185 Roma, Italy

³ Department of Astronomy, University of Massachusetts, 710 North Pleasant Street, Amherst, MA 01003

⁴ MPA Max-Planck-Institute für Astronomie, Königstuhl 17, 69117 Heidelberg, Germany

⁵ INAF - Osservatorio Astronomico di Trieste, Via G.B. Tiepolo 11, 34131 Trieste, Italy

⁶ Dip. di Fisica, Università Tor Vergata, Via della Ricerca Scientifica 1, 00133 Roma, Italy

⁷ INFN-Roma Tor Vergata, Via della Ricerca Scientifica 1, 00133 Roma, Italy

Received ; accepted

ABSTRACT

Aims. The goal of this work is to infer the star formation properties and the mass assembly process of high redshift ($0.3 \leq z < 2.5$) galaxies from their IR emission using the $24 \mu\text{m}$ band of MIPS-Spitzer.

Methods. We used an updated version of the GOODS-MUSIC catalog, with multi-wavelength coverage from 0.3 to $24 \mu\text{m}$ and spectroscopic or accurate photometric redshifts. We describe how the catalog has been extended with the addition of mid-IR fluxes derived from the MIPS $24 \mu\text{m}$ image. We compared two different estimators for the star formation rate (SFR hereafter). One is the total infrared emission as derived from $24 \mu\text{m}$, estimated using both synthetic and empirical IR templates. The other one is a multi-wavelength fit to the full galaxy SED, which automatically accounts for dust reddening and age–star formation activity degeneracies. With both estimates we computed the SFR density and the specific SFR.

Results. We show that the two SFR indicators are roughly consistent, once the involved uncertainties are taken into account. However, they show a systematic trend, with IR-based estimates exceeding the fit-based ones for increasing star formation rate. With this new catalog, we show that: *a*) At $z > 0.3$, the star formation rate is well correlated with stellar mass, and this relationship seems to steepen with redshift if one relies on the IR–based estimates of the SFR; *b*) The contribution to the global SFRD by massive galaxies increases with redshift up to ≈ 2.5 , faster than for galaxies of lower mass, but appears to flatten at higher z ; *c*) Despite this increase, the most important contributors to the SFRD at any z are galaxies around, or immediately below, the characteristic stellar mass; *d*) At $z \approx 2$, massive galaxies are actively star-forming, with a median $\text{SFR} \approx 300 M_{\odot} \text{yr}^{-1}$. During this epoch, they assemble a substantial part of their final stellar mass; *e*) The specific SFR (SSFR) shows a clear bimodal distribution.

Conclusions. The analysis of the SFR density and the SSFR seems to support the *downsizing* scenario, according to which high mass galaxies have formed their stars earlier and faster than their low mass counterparts. A comparison with recent renditions of theoretical simulations of galaxy formation and evolution shows that these models follow the global increase of the SSFR with redshift and forecast the existence of quiescent galaxies even at $z > 1.5$. However, the average SSFR is systematically under-predicted by all the models considered.

Key words. Galaxies: evolution - Galaxies: high-redshift - Galaxies: fundamental parameters - Galaxies: photometry - Galaxies: starburst

1. Introduction

Answering the basic questions about birth, formation, mass buildup and evolution of galaxies throughout the cosmic time is one of the major goals of observational extragalactic astronomy.

In the past years this issue has been approached from a double point of view. Many previous works have measured a rapid evolution of the stellar mass density between $z \sim 1$ and $z \sim 3$ (Dickinson et al. 2003; Fontana et al. 2003, 2004; Glazebrook et al. 2004; Drory et al. 2004; Fontana et al. 2006; Rudnick et al. 2006; Papovich et al. 2006; Yan et al. 2006; Pozzetti et al. 2007) and have demonstrated that a substantial fraction (30-50%) of the stellar mass formed at that epoch. The differential evolution of the galaxy stellar mass function, according to which massive galaxies evolve very fast up to $z \sim 1.5$

and then much mildly up to the present epoch, while less massive galaxies keep evolving, suggests that massive galaxies must have been already formed by $z \sim 1.5$. Besides, several groups (e.g. Faber et al. 2007; Brown et al. 2007) studied the evolution of massive galaxies at $z \lesssim 1$, and their migration from the blue cloud to the red sequence. It is worth noting that optical observations (Bell et al. 2004; Zucca et al. 2006) suggest that the number of massive galaxies, as well as the stellar mass on the red sequence, nearly doubled since $z \sim 1$, in qualitative agreement with the hierarchical merging scenario.

As a parallel line of study, an analysis of the rate at which galaxies are forming stars through different epochs showed that they are actually experiencing an extremely active phase in the same redshift range (e.g. Lilly et al. 1996; Madau et al. 1996; Steidel et al. 1999; Hopkins 2004; Hopkins & Beacom 2006; Daddi et al. 2007b). Galaxies seem to form their stars following the so-called *downsizing* scenario, in which the star for-

mation shifts from high mass to low mass galaxies as redshift decreases. According to this picture, which was first introduced by Cowie et al. (1996), who studied the evolution of the K_s band luminosity function with redshift, most massive galaxies assemble their mass both earlier and more quickly than their lower mass counterparts, which, conversely, continue to form stars until recent epochs. Later on, many other groups (e.g., Brinchmann & Ellis 2000; Fontana et al. 2003; Feulner et al. 2005; Pérez-González et al. 2005; Papovich et al. 2006; Damen et al. 2009) derived confirmations of a *downsizing* behaviour from the study of the specific star formation rate, defined as the star formation rate per unit mass, at different redshifts. However, it is worth mentioning that deep radio observations (Dunne et al. 2009) apparently do not confirm this scenario. The *downsizing* picture is only apparently contradicting the hierarchical growth scenario: in fact, the most massive structures we see today result from merging processes between smaller structures which were sitting on large scale overdensities and have collapsed when the Universe was much younger than today.

To reproduce such an early formation of massive galaxies (see Thomas et al. 2005), already “red and dead” at high z , theoretical models had to introduce very efficient star formation processes together with their suppression by means of Active Galactic Nuclei and supernovae quenching of the cooling flows (Menci et al. 2006; Kitzbichler & White 2007; Bower et al. 2006; Croton et al. 2006; Nagamine et al. 2006; Monaco et al. 2007), gravitational heating (Khochfar & Ostriker 2008; Johansson et al. 2009) or shock heating (Dekel & Birnboim 2006). Such models slightly differ in their predictions mainly because they adopt different processes to shut down the star formation.

Both stellar masses and star formation rate estimates are affected by a number of uncertainties. The measure of the star formation rate (SFR) is especially difficult to handle. The high amount of energy produced by newly born stars is emitted throughout the galaxy spectral energy distribution (SED), from X-rays to radio frequencies. Evidently, it is impossible to directly measure the total light emitted by young and massive stars, and calibration factors and corrections are required to estimate it from any of these frequency ranges (Kennicutt 1998; Bell 2003; Calzetti 2008). One of the most used estimators is the UV rest-frame band, where young and massive stars emit most of their light. However, dust absorbs, reprocesses and re-radiates UV photons at near-to-far IR wavelengths. Hence, the reliability of UV luminosity as a SFR tracer depends on large and uncertain corrections relying upon the dust properties, which are not clearly known yet (Calzetti et al. 1994; Calzetti 1997, 2001). Moreover, the UV-upturn at λ shortward of 2500 Å (e.g. Han et al. 2007), especially in elliptical galaxies, can potentially bias the SFR estimate at very low redshift. Since the most intense star formation episodes are expected to happen in dusty regions, most of the power coming from star-forming (SF) galaxies is emitted in this wavelength range, and the dust emission peak is the dominant component of SF galaxies SEDs (Adelberger & Steidel 2000; Calzetti et al. 2000). Thus, a frequent approach consists in adopting a conversion to transform the total emitted IR luminosity (L_{IR} hereafter) into a star formation rate estimation which is not affected by dust obscuration (Kennicutt 1998).

The total infrared luminosity is generally estimated through the comparison between observed SEDs and synthetic templates, although sometimes empirical conversions have been used (Takeuchi et al. 2005; Bavouzet et al. 2007). A vari-

ety of different libraries are used for this purpose (e.g., Chary & Elbaz 2001; Dale & Helou 2002; Lagache et al. 2003; Siebenmorgen & Krügel 2007, and so on). A notable limitation to the reliability of IR-based SFR tracers concerns obscured AGNs. In these objects, indeed, the IR emission is caused by matter accretion on the central black hole rather than by dust heating from young stars.

In this paper we use the GOODS-MUSIC catalog to investigate properties of star-forming galaxies up to redshift 2.5 and describe the mass assembly process from their mid-IR emission. The paper is organized as follows. In Sect. 2, we remind the basic features of the GOODS-MUSIC dataset and explain the innovations concerning its latest version, and we explain how it has been updated with the addition of the 24 μm photometric band. We derive and compare star formation rates from IR- and fit-based estimators in Sect. 3. In Sect. 4, we present a study on the mass assembly process in the high redshift Universe and a comparison with theoretical models predictions. Finally, we summarize our work and our conclusions in Sect. 5. In Appendix A we describe in more details how we convert mid-IR fluxes into total infrared luminosities and we show a comparison between the different templates used, and in Appendix B we present the error analysis performed on the fit-based SFR estimates.

Throughout this work, unless otherwise stated, we assume a Salpeter (1955) initial mass function (IMF) and we adopt the Λ -CDM concordance cosmological model ($H_0 = 70 \text{ km/s/Mpc}$, $\Omega_M = 0.3$ and $\Omega_\Lambda = 0.7$).

2. The data sample

2.1. The new GOODS-MUSIC sample

We present and use here an updated version of the multi-colour GOODS-MUSIC sample (GOODS Multicolour Southern Infrared Catalog; Grazian et al. 2006), extracted from the public data of the GOODS-South survey (Giavalisco et al. 2004). In the following, we shall refer to this version of the catalog as GOODS-MUSIC v2, to differentiate it from the former public version, which is named v1 hereafter. The new version is also made publicly available¹.

The 15-bands multi-wavelength coverage ranges from 0.35 to 24 μm , as a result of the combination of images coming from different instruments (2.2ESO, VLT-VIMOS, ACS-HST, VLT-ISAAC, Spitzer-IRAC, Spitzer-MIPS). Such catalog covers an area of $\sim 143.2 \text{ arcmin}^2$ located in the Chandra Deep Field South and it is made of 15208 sources. After culling Galactic stars, it contains 14999 objects selected in the z band or in the K_s band or at 4.5 μm .

The whole catalog has been cross-correlated with spectroscopic catalogs available to date, and a spectroscopic redshift has been assigned to $\sim 12 \%$ of sources. For all other objects we have computed well calibrated photometric redshifts using a standard χ^2 minimization technique over a large set of synthetic spectral templates.

The previous version of the catalog and the procedures adopted to extract photometric redshifts and physical properties for each object are described at length in Grazian et al. (2006) and Fontana et al. (2006). With respect to the previous catalog, we have performed a set of improvements to the optical–near-IR data, the major being:

¹ The catalog is available in electronic form at the CDS via anonymous ftp to cdsarc.u-strasbg.fr (130.79.128.5) or via <http://cdsweb.u-strasbg.fr/cgi-bin/qcat?J/A+A/>. It is also possible to download the catalog at the WEB site <http://lbc.mporzio.astro.it/goods>.

- In addition to objects selected in the ACS z and in the ISAAC K_s bands, we have also included objects selected on the IRAC 4.5 μm image, hence including sources which are detected at 4.5 μm but very faint or undetected even in the K_s band. A full description of these objects is beyond the scope of the present paper and will be presented elsewhere.
- We have revised the photometry in the four IRAC bands using an updated version of the PSF-matching kernels, as released by the Spitzer Science Center. As a consequence, we also adopted a larger kernel, to fully account for the large tails of the IRAC PSFs.
- We have adopted a revised procedure for estimating the background in the IRAC images. Using the objects' positions and IRAC fluxes from the GOODS-MUSIC v1 catalog, we have created realistic simulated images in the four IRAC bands by smoothing sources to the nominal IRAC PSFs. An accurate background estimation was performed by subtracting these simulated images from the original ones and by linearly interpolating the residual emission. Since the average value of the apparent IRAC background is negative, this has led to an increase in the adopted background, with respect to the GOODS-MUSIC v1 version.
- These two changes have modified the IRAC photometry. Because of the new kernels, the brightest objects have a higher flux, and have a typical offset in the magnitudes of 0.23, 0.14, 0.22, 0.35 respectively in the 3.6, 4.5, 5.8 and 8 μm images, with respect to the GOODS-MUSIC v1 catalog, in agreement with the recent analysis of Wuyts et al. (2008). This effect is largely mitigated for fainter galaxies, since the higher background now adopted has led to an underestimate of their fluxes.
- Overall, the revised IRAC photometry has a modest impact on the estimate of photometric redshifts, since $\langle z_{\text{phot v2}} - z_{\text{phot v1}} \rangle \sim 0.01 \pm 0.16$ on the whole sample and $\sim 0.01 \pm 0.03$ when a 3σ -clipping analysis is performed (see also Wuyts et al. (2008)).
- A more informative test on the accuracy of photometric redshifts comes from the enlargement of the sample of galaxies with spectroscopic redshifts, that we obtained by adding new spectra from recent public surveys (Vanzella et al. 2008; Popesso et al. 2009). In addition, we have also had access to the spectra of the GMASS survey (Cimatti et al. 2008), prior to their publication. The final sample now includes 1888 galaxies, three times larger than the spectroscopic sample in Grazian et al. (2006). The additional spectra are mostly relative to galaxies that are both fainter and at higher redshifts than in the original sample. Without significant refinements in the adopted templates, we then find that the absolute scatter $|\Delta z| = |z_{\text{spe}} - z_{\text{phot}}|/(1 + z_{\text{spe}})$ has a slightly larger average value. Quantitatively, the average absolute scatter is now $\langle |\Delta z| \rangle = 0.06$, instead of 0.045 obtained for the GOODS-MUSIC v1 catalog. However, when only the brightest galaxies are considered, we find comparable values with respect to Grazian et al. (2006) ($\langle |\Delta z| \rangle = 0.043$). We have verified that this is due to an increased number of outliers, as shown by a 3σ -clipping analysis, which provides $\langle |\Delta z| \rangle = 0.027$ and 0.032 for the complete datasets of v1 and v2 catalogs respectively.
- We have removed Galactic stars and performed a more careful selection of the galaxy sample to identify AGN sources. For the latter, we have first removed all objects whose spectra show Broad Line emission. Then, we have cross-correlated our catalog with the X-ray catalog of Brusa et al. (in prep.), and removed all X-ray detected sources whose flux is dom-

inated by an unresolved central source. Such sources typically have spectra classified as Narrow Line AGNs. The optical morphologies of all remaining X-ray sources do not show a dominating central point like source, and – where available – have typically spectra classified as Emission Line star-forming galaxies. Such objects have been kept in our galaxy sample.

The major new ingredient of this new version of the GOODS-MUSIC catalog, however, is the inclusion of the 24 μm photometry for all galaxies in the sample, which is the main focus of the present paper. We describe the adopted procedures and results in the following.

2.2. MIPS 24 μm catalog

We have extended the GOODS-MUSIC catalog with the addition of the mid-IR fluxes derived from the public 24 μm image of the Multiband Imager Photometer for Spitzer (MIPS, Rieke et al. 2004) on-board Spitzer Space Telescope. As in the case of the IRAC images, given the very large PSF of this image (~ 5.2 arcsec), to properly detect and de-blend objects we have employed a PSF-matching technique, which is performed by the software ConvPhot (De Santis et al. 2007). It measures colours between two images having different qualities by exploiting the spatial and morphological information contained in the higher resolution image.

When applying ConvPhot to our case, each object is extracted from the high resolution z band ACS-HST (PSF $\sim 0.12''$) image, which is used as a *prior* to extract the objects' positions, it is filtered with a convolution kernel, and it is finally scaled through a χ^2 minimization over all image pixels to match the intensity in the MIPS image. To fully use the positional information of the ACS images, and keep the consistency with the z -selected sample, we keep using the z band ACS-HST as a *prior*, augmented by artificial objects placed where galaxies detected only in K_s or 4.5 μm are located.

In our case, the MIPS-Spitzer and ACS-HST images have pixel scales of 1.2 and 0.03 arcsec/pixel, that would make impracticable the use of ConvPhot even with fast workstations. To make the computation feasible, we rebinned the ACS detection image by a factor 8×8 (0.24 arcsec/pixel).

In regions where the crowding of the z -detected sources is large, the fit may become unconstrained or degenerate due to the large size of the MIPS PSF. To prevent this, we put an additional constraint on the fitted fluxes that must be non-negative. For the objects whose flux is forced to zero, we provide an upper limit derived from the analysis of the mean rms in the object area.

The behaviour of ConvPhot in such extreme applications has been tested with several simulations, which can be found in De Santis et al. (2007). These tests indicate that estimated magnitudes are not biased by the different qualities of the two images and by the undersampling of the high resolution image after re-binning.

Finally, from visual inspection of sources with unusual colours, we removed from the catalog ~ 30 objects whose flux was not correctly assigned. We have also verified, by examination of the residuals, that there is not any significantly bright source in MIPS image apart from the ones considered. We end up with 3313 ($\sim 22\%$ of total) detected objects and 11841 ($\sim 78\%$) 1σ upper limits.

Despite the validation tests gave satisfying results, we must stress that the intrinsic limitations due to the poor resolution of the MIPS image cannot be completely overcome, in partic-

ular for sources which are blended even in the *detection* image, i.e. sources whose profiles overlap in the ACS z image. In this case, the separation between the two – or more – objects can become even smaller than the positional accuracy of the MIPS images, and the association between the z -detected and the MIPS sources relies on the accuracy of the astrometric solution. To allow a check against possible misidentifications, we have associated each source with a flag to quantify the number of possible contaminants, at different distances. Such flag is attached with the public catalog and we warn the user to check against possible systematic errors. The results that we shall present in the following are not sensitive to the inclusion of the most blended sources, which therefore have not been removed.

It may be interesting to show the effect of this procedure on the $24\ \mu\text{m}$ number counts, shown in Fig. 1. We present both the counts derived by ConvPhot as well as those obtained by a SExtractor catalog which has been produced by adopting corrected aperture magnitudes at 6 arcsec. The blue shaded region shows $24\ \mu\text{m}$ counts from Papovich et al. (2004). They counted sources in five different fields (CDF-S among them) using DAOPHOT software. The green solid line (error bars are not large enough to be seen) represents Shupe et al. (2008) counts in the SWIRE field performed by SExtractor. ConvPhot (black dots) gives consistent results with previous works of other authors up to the lowest fluxes and with our SExtractor catalog (red circles) at $F \gtrsim 100\ \mu\text{Jy}$.

The agreement at bright fluxes confirms the simulations and validation tests presented in De Santis et al. (2007), showing that the fluxes estimated by ConvPhot agree with those estimated by a self-standing detection with SExtractor for sources that are not severely blended. For the blended fraction of the objects, however, the fluxes estimated by ConvPhot can be slightly lower, since part of the flux is ascribed to the fainter contaminants, which are not detected in the $24\ \mu\text{m}$ image alone.

It is more interesting to look at the behaviour at faint fluxes, where the a priori knowledge of the object position, due to the use of the z , K_s and $4.5\ \mu\text{m}$ images for the detection, allows to push the flux estimate at much fainter limits, reducing the effects of blending and confusion. As expected, indeed, SExtractor counts drop off at $\sim 100\ \mu\text{Jy}$, where the confusion limit prevents the detection of fainter sources, while ConvPhot allows to go much deeper. ConvPhot number counts present a double slope, with a break point located at $\sim 100\ \mu\text{Jy}$, which we consider an intrinsic property of the sample. The slope and the normalization at the faint end agree with the estimates of Papovich et al. (2004), who carefully computed a correction for the incompleteness due to poor resolution at faint limits. Papovich et al. (2004) and following papers estimated that the source detection in MIPS-CDFS is 80% complete at $83\ \mu\text{Jy}$, that typically corresponds to $S/N \sim 28\text{--}30$ in our fitting procedure. For consistency with such works, we will therefore distinguish between objects with fluxes above this limit and those detected at lower S/N , down to fluxes $\sim 20\ \mu\text{Jy}$, which corresponds to our flux counts limit. The median S/N at this flux limit is $\sim 6\text{--}7$, although a tail is present at lower values of S/N caused by the sources blending. Nevertheless, such tail includes only a small number of objects.

Finally, we cross-correlated our $24\ \mu\text{m}$ catalog both with FIREWORKS catalog (Wuyts et al. 2008) and with the one released by the GOODS Team² (Chary 2006), who adopted a similar source extraction technique. The overall agreement is good, with a small offset in both

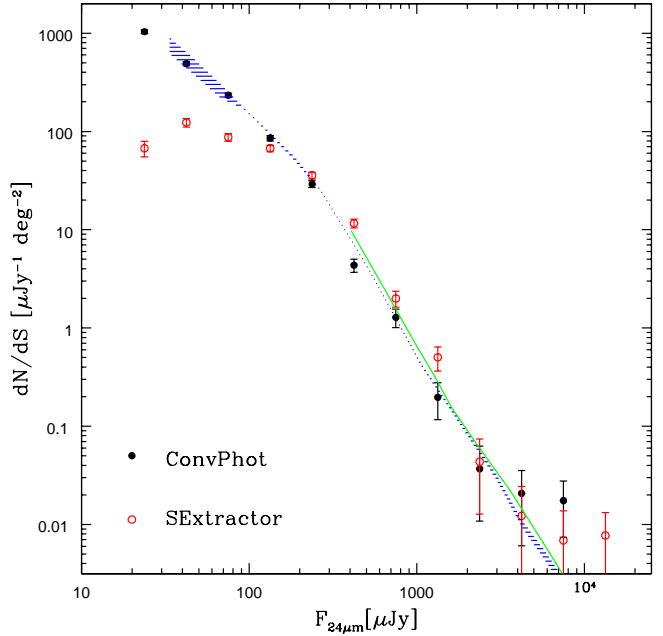


Fig. 1. $24\ \mu\text{m}$ flux number counts measured by ConvPhot (black filled circles) and SExtractor (red empty circles). Error bars have been computed as the square root of the number of objects in each bin. We compared our results to Papovich et al. (2004) and Shupe et al. (2008) $24\ \mu\text{m}$ counts (blue and green shaded region).

cases ($\langle F_{24\mu\text{m}} \text{ GOODS-MUSIC} / F_{24\mu\text{m}} \text{ FIREWORKS} \rangle \sim 1.2$ and $\langle F_{24\mu\text{m}} \text{ GOODS-MUSIC} / F_{24\mu\text{m}} \text{ DR3} \rangle \sim 0.91$).

2.3. The data selection

As pointed out above, we removed from our catalog Galactic stars and both spectroscopic or X-ray detected AGN sources. Moreover, we only consider the redshift range $0.3\text{--}2.5$. From such sample, we shall regard the following two subsamples:

- the purely K_s -selected sample (subsample A), made of 2602 galaxies. Of these, 983 (379) are $24\ \mu\text{m}$ detections with $F_{24\mu\text{m}} > 20$ (83) μJy and 1619 have been assigned an upper limit;
- the sample originated by the combination of the following cuts: $z < 26$ or $K_s < 23.5$ or $m_{4.5} < 23.2$ (subsample B). It includes 7923 galaxies, of which 1167 (416) are $24\ \mu\text{m}$ detections with $F_{24\mu\text{m}} > 20$ (83) μJy and 6756 are upper limits.

3. Comparison between SFR indicators

3.1. SFR estimators: IR-, fit- and UV-based SFR

Under the assumption that most of the photons coming from newly formed stars are absorbed and re-emitted by dust, the mid-IR emission is in principle the most sensitive tracer of the star formation rate. In addition, a small fraction of unhindered photons will be anyway detected at UV wavelengths. A widely used SFR indicator is therefore a combination of IR and UV luminosity, which supplies complementary knowledge about the star formation process (Iglesias-Páramo et al. 2006; Calzetti et al. 2007). For $24\ \mu\text{m}$ detected sources, we estimate the instant-

² GOODS-South MIPS $24\ \mu\text{m}$ source list v0.91 from GOODS data release (DR3).

neous SFR using the same calibration as Papovich et al. (2007) and Bell et al. (2005):

$$\text{SFR}_{\text{IR+UV}}/M_{\odot}\text{yr}^{-1} = 1.8 \times 10^{-10} \times L_{\text{bol}}/L_{\odot} \quad (1)$$

$$L_{\text{bol}} = (2.2 \times L_{\text{UV}} + L_{\text{IR}}) \quad (2)$$

L_{IR} has been computed by fitting $24 \mu\text{m}$ emission to Dale & Helou (2002) (DH hereafter) synthetic templates, widely adopted in the recent literature. In appendix A, we present a comparison among the resulting L_{IR} predicted by different model libraries (Chary & Elbaz 2001; Polletta et al. 2007).

We include the rest-frame UV luminosity, uncorrected for extinction, derived from the SED fitting technique, $L_{\text{UV}} = 1.5 \times L_{2700\text{\AA}}$. This latter amount, albeit often negligible, accounts for the contribution from young unobscured stars.

We then applied a lowering correction to the estimate obtained by eq. 1 following Papovich et al. (2007). They find that $24 \mu\text{m}$ flux, fitted with the same DH library, overestimates the SFR with respect to the case where longer wavelengths (70 and $160 \mu\text{m}$ MIPS bands) are considered as well, and they correct the trend using an empirical second-order polynomial. In appendix A we show a further confirmation for applying this correction: for bright sources, L_{IR} estimated by synthetic models has values which are up to a factor 10 higher compared to L_{IR} predicted by the empirical library of Polletta et al. (2007). Similar results have also been published by Bavouzet et al. (2007) and Rieke et al. (2009).

In the following, we will refer to the estimate in eq. 1 as $\text{SFR}_{\text{IR+UV}}$.

A complementary approach to estimate the star formation rate, as well as other galaxy physical properties (such as mass, age, dust extinction and so on), is the SED fitting. A grid of spectral templates is computed from standard spectral synthesis models, and the expected magnitudes in our filter set are calculated. The derived template library is compared with the available photometry and the best fitting template is adopted according to a χ^2 minimization. During the fitting process the redshift is fixed to the spectroscopic or photometric one. The physical parameters associated to each galaxy are obtained from the best fitting template up to $5.5 \mu\text{m}$ rest-frame. This analysis assumes that the overall galaxy SED can be represented as a purely stellar SED, extincted by a single attenuation law, and that the relevant $E(B-V)$ and basic stellar parameters (mostly age and star formation history, but also metallicity) can be simultaneously recovered with a multi-wavelength fit. It is to be noted that parameter degeneracies can not be completely removed, especially at high redshift. Previous studies (Papovich et al. 2001; Shapley et al. 2001, 2005) demonstrated that, while stellar masses are well determined, the SED fitting procedure does not strongly constrain star formation histories at high redshifts, where the uncertainties become larger due to the SFR–age–metallicity degeneracies. For this reason, the uncertainties associated to the SFR values estimated from the SED fitting are larger than those associated to the IR tracer.

In our analysis, we estimated star formation rates (along with stellar masses) using Bruzual & Charlot (2003) synthetic models, fitting the whole 14 bands photometry (from the U band to $8 \mu\text{m}$). We parameterize the star formation histories with a variety of exponentially declining laws (with timescales τ ranging from 0.1 to 15 Gyr), metallicities (from $Z = 0.02 Z_{\odot}$ to $Z = 2.5 Z_{\odot}$) and dust extinctions ($0 < E(B-V) < 1.1$, with a Calzetti or Small Magellanic extinction curve). Details are given in Table 1 of Fontana et al. (2004), in Fontana et al. (2006) and in Grazian et al. (2006, 2007). The only difference with respect

to these recipes is the adoption of a minimum age of 0.1 Gyr. Below this value, the relation between UV luminosity and star formation rate changes rapidly with the age of the stellar population, leading to very large values of inferred SFRs. We are aware that exponential star formation histories may not be the best choice in some cases. However, modeling in detail the star formation history of our galaxies is beyond the scope of the present paper, whose aim is to compare the star formation rates derived from the IR emission with the ones based on the widely used SED fitting procedures.

We will refer to this SFR estimation as SFR_{fit} .

We have also fitted our data using the more recent Maraston (2005) and Charlot & Bruzual (in prep., see Bruzual 2007a,b), including an improved TP-AGB stars treatment. The stellar mass estimates inferred using these new models are presented in Salimbeni et al. (2009) and are lower by 0.2 dex approximately compared to the ones computed with Bruzual & Charlot (2003) models. However, the extrapolated SFR values induce a significant overestimate (especially in the case of Maraston (2005) models) in the measure of the SFR density that we present in Sect. 4.2. We suspect that part of this discrepancy is due to peculiar shapes in the near-IR side of the spectrum, which likely cause the worse χ^2 that we measure compared to the one computed using Bruzual & Charlot (2003) models. Since a proper comparison between stellar population models is out of the scope of this paper, and pending further tests on these new models, we keep adopting the widely used Bruzual & Charlot (2003) template library and refer to possible future works for more details on this point.

At $z > 1.5$, it is possible to obtain an independent estimate of the SFR using the observed L_{1500} and the observed slope of the UV continuum to estimate the $E(B-V)$, rather than the multi-wavelength fit. In the following we shall use the conversions adopted by Daddi et al. (2004), culling a sample of BzK–SF galaxies from our catalog and deriving the relevant SFR using the Daddi et al. (2004) scaling relations $\text{SFR}_{\text{UV}}/M_{\odot}\text{yr}^{-1} = L_{1500}/L_0$, with $L_0 = 8.85 \times 10^{27} \text{erg s}^{-1} \text{Hz}^{-1}$, and $A_{1500} = 10 \times E(B-V)$, where $E(B-V) = 0.25(B-z+0.1)_{\text{AB}}$.

We will refer to this SFR estimation as SFR_{1500} .

For clarity, SFRs lower than $0.01 M_{\odot}\text{yr}^{-1}$ have been forced to $0.01 M_{\odot}\text{yr}^{-1}$ in the following analysis.

3.2. Comparison between IR– and fit–based tracers

We can now discuss the consistency of the different SFR estimates. We will use in this section the K_s –selected sample (sub-sample A) to ensure a proper sampling of the full SED, e.g. to be sure that all the bands, or most of them, are available for the fitting procedure.

We start from the redshift range 0.3 – 1.5, plotting in Fig. 2 the comparison between $\text{SFR}_{\text{IR+UV}}$ and SFR_{fit} . We include both the $24 \mu\text{m}$ detected galaxies as well as the undetected ones, for which only upper limits on $\text{SFR}_{\text{IR+UV}}$ can be obtained. These upper limits are somewhat misleading for the interpretation of the figure: since the SED fitting can reach lower nominal values for the SFR, the scatter in SFR_{fit} seems to be larger than that in $\text{SFR}_{\text{IR+UV}}$.

Given the many uncertainties involved in both estimators, the overall consistency between them appears reassuring. Apart from offsets and other systematics, that we shall discuss below, the majority of galaxies are assigned a consistent SFR, and the number of severe inconsistencies is small. Such inconsistencies may be due to two different origins.

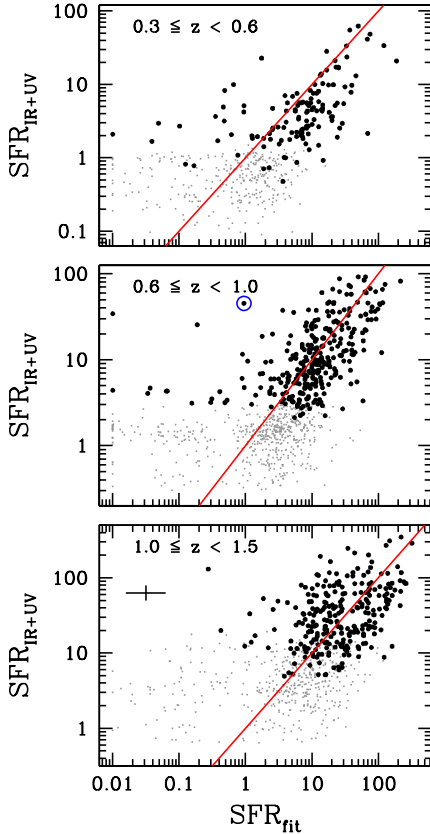


Fig. 2. Relation between $\text{SFR}_{\text{IR+UV}}$ and SFR_{fit} in three redshift bins for the whole K_s -selected sample. Filled black dots are for the $F_{24\mu\text{m}} > 20 \mu\text{Jy}$ subsample; small gray dots refer to galaxies undetected at $24 \mu\text{m}$, and must be regarded as upper limits. The blue circle identifies an obscured AGN candidate, selected according to a similar technique as the one presented in Fiore et al. (2008) (see text). The red line defines the locus $\text{SFR}_{\text{IR+UV}} = \text{SFR}_{\text{fit}}$. The typical uncertainties associated with both estimates is shown in the lower panel. The intrinsic parameter degeneracy involved with the SED fitting procedure is responsible for the larger uncertainties associated with SFR_{fit} . Units are $M_\odot\text{yr}^{-1}$.

On one side, galaxies with SFR_{fit} much larger than $\text{SFR}_{\text{IR+UV}}$ can in principle arise from incorrect fitting of red galaxies. For such objects, the SED fitting could erroneously assign a large amount of dust to an otherwise dust-free, passively evolving population. Despite the relatively large number of passively evolving galaxies at $z < 1.5$, the number of these misidentifications is very small at $z < 1$, and low even at $z = 1 - 1.5$.

On the other side, galaxies with $\text{SFR}_{\text{IR+UV}} \gg \text{SFR}_{\text{fit}}$ can be obtained either when the opposite misidentification occurs (e.g. for dusty star-forming galaxies fitted with a passively evolving SED) or, more interestingly, when the mid-IR emission is due to additional processes, not observable in the UV/optical regime. Typical cases are AGN emission or additional star formation activity completely dust enshrouded. At $z < 1.5$, such objects are again very rare in our sample. In particular, the SFR of the very few galaxies with $\text{SFR}_{\text{IR+UV}} \approx 2 - 6 M_\odot\text{yr}^{-1}$ and $\text{SFR}_{\text{fit}} < 1 M_\odot\text{yr}^{-1}$ at $z < 1$ is likely overestimated, resulting from the incorrect application of a star-forming template to a more quiescent galaxy (see Fig. A.3).

For a more detailed discussion on the robustness of the fit-based SFR estimates, the related error analysis and χ^2 contours, we refer the reader to Appendix B.

The existing systematic trends can be better appreciated by looking at Fig. 3 (a), where we plot the $\text{SFR}_{\text{IR+UV}}/\text{SFR}_{\text{fit}}$ ratio for the $24 \mu\text{m}$ detected sample. First, we note that the scatter in the $\text{SFR}_{\text{IR+UV}}/\text{SFR}_{\text{fit}}$ distribution widens with redshift. This is probably due to a combination of effects: as we move to high redshifts, galaxies become intrinsically fainter and the rest-frame spectral coverage gets narrower, making the SED fitting more uncertain; likewise, $24 \mu\text{m}$ based indicators could become more uncertain as the filter moves away from the rest-frame mid-IR and approaches the PAH region.

More interestingly, a correlation between the $\text{SFR}_{\text{IR+UV}}/\text{SFR}_{\text{fit}}$ ratio and $\text{SFR}_{\text{IR+UV}}$ can be observed. Indeed, if we focus our attention on galaxies which form from 10 to $100 M_\odot\text{yr}^{-1}$, the $\text{SFR}_{\text{IR+UV}}/\text{SFR}_{\text{fit}}$ distribution (black histograms) is centered at unity and fairly symmetric. Conversely, galaxies with a milder activity (gray shaded histograms), present lower $\text{SFR}_{\text{IR+UV}}/\text{SFR}_{\text{fit}}$ ratios, and a first hint of highly star-forming galaxies (red horizontally shaded histogram), i.e. objects making more than $100 M_\odot\text{yr}^{-1}$, shows higher $\text{SFR}_{\text{IR+UV}}/\text{SFR}_{\text{fit}}$ ratios.

The same systematic effects are seen at higher redshift. The upper panel of Fig. 3 (b) shows the ratio $\text{SFR}_{\text{IR+UV}}/\text{SFR}_{\text{fit}}$ in the $1.5 - 2.5$ range. It is immediately clear that the spread is larger than at lower redshifts, and that a large number of objects with $\text{SFR}_{\text{IR+UV}}/\text{SFR}_{\text{fit}} \gg 1$ is observed. The observed spread is not surprising, since a similar disagreement, up to two orders of magnitude in single galaxies at comparable redshifts, has already been noticed by the similar analysis of Papovich et al. (2006). At these redshifts, the faintness of the galaxies and the large k -corrections in the mid-IR are clearly even more effective in increasing the noise in both estimates. The factor ~ 2 shift of the distribution of galaxies with SFR between 10 and $100 M_\odot\text{yr}^{-1}$ is consistent with the uncertainty associated with the spectral library used to compute L_{IR} (see Appendix A).

It is therefore interesting to compare these estimates with the pure UV-based SFR_{1500} , described above. The relation between $\text{SFR}_{\text{IR+UV}}$ and $\text{SFR}_{\text{IR+UV}}/\text{SFR}_{1500}$ ratio is shown in the lower panel of Fig. 3 (b). Following Daddi et al. (2004), we applied this recipe only to the sample of BzK-SF in the redshift range of interest. The scatter is significantly reduced compared to the upper panel, but the same trend to present an IR excess still appears for highly star-forming objects.

To some extent, the excess of mid-IR derived star formation rate is most likely due to the presence of highly obscured AGNs. Daddi et al. (2007a) made the assumption that all the mid-IR excess objects drawn from the BzK-SF sample (i.e. all objects of lower panel of Fig. 3 (b) with $\text{SFR}_{\text{IR+UV}}/\text{SFR}_{1500} > 3$) are powered by obscured AGNs. Following a different approach, Fiore et al. (2008) identified a population of highly obscured AGNs candidates in the whole K_s -selected sample, selected by their very red spectrum ($F_{24\mu\text{m}}/F(R) > 1000$ and $R - K_s > 4.5$) (see also Dey et al. 2008). In this work, in order to use fluxes directly measured in our catalog, we selected the very same objects following the criterium $F_{24\mu\text{m}}/F(I) > 1000$ and $I - K_s > 4.5$, which we checked to be consistent with that used in Fiore et al. (2008). Such objects are shown as blue open circles in Figs. 2 and 3.

The presence of highly obscured AGNs could also induce the observed trend in the $\text{SFR}_{\text{IR+UV}}/\text{SFR}_{\text{fit}}$ ratio, since they are expected to be harboured in high mass galaxies, that are on average highly star-forming. Indeed, a correlation between the fraction

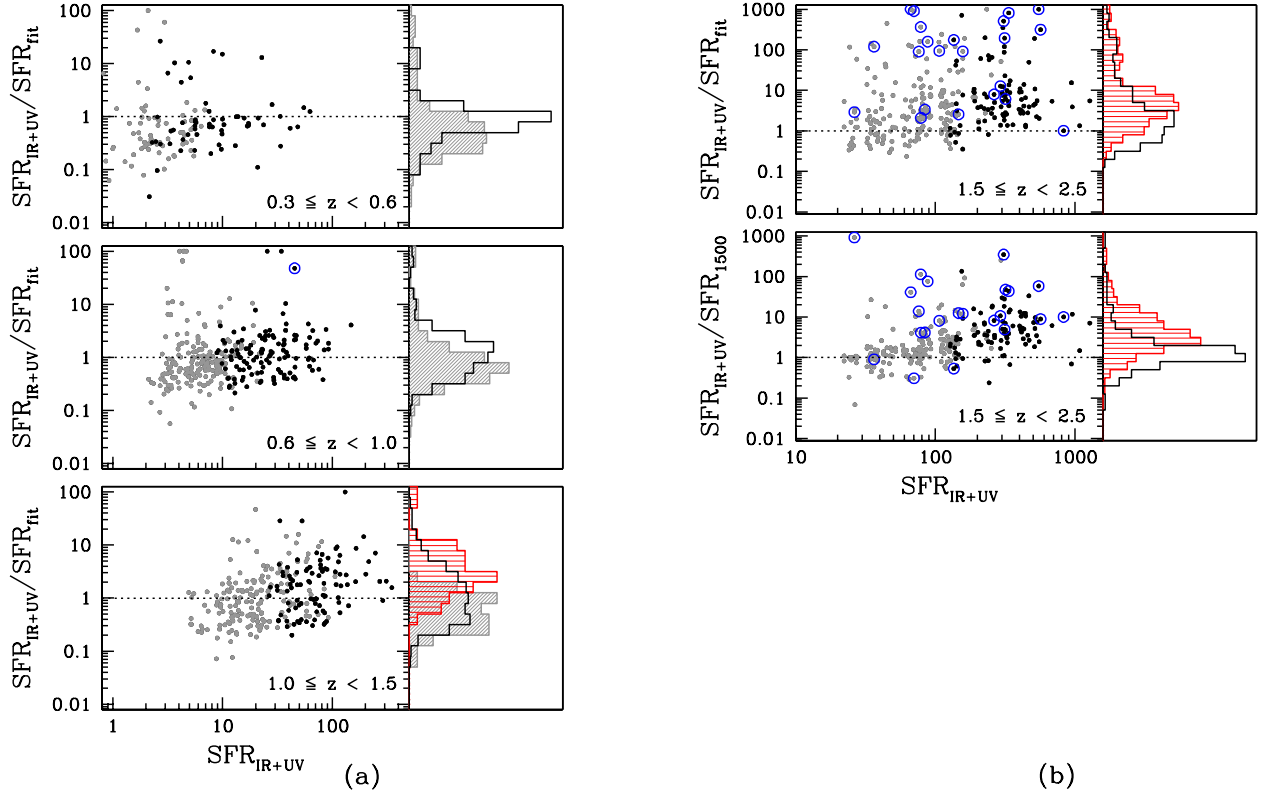


Fig. 3. Left panels in (a) and left top panel in (b): relation between $\text{SFR}_{\text{IR+UV}}/\text{SFR}_{\text{fit}}$ ratio and $\text{SFR}_{\text{IR+UV}}$ in the different redshift bins for the $F_{24\mu\text{m}} > 83 \mu\text{Jy}$ (black dots) and $20 < F_{24\mu\text{m}} [\mu\text{Jy}] \leq 83$ detected galaxies (gray dots); blue circles identify obscured AGN candidates, selected according to a similar technique as the one presented in Fiore et al. (2008) (see text). Left middle panel in (b): relation between $\text{SFR}_{\text{IR+UV}}/\text{SFR}_{1500}$ ratio and $\text{SFR}_{\text{IR+UV}}$ in the redshift bin 1.5–2.5 for the subsample of BzK-SF galaxies; symbols are as in the other panels. Right panels in (a) and (b): black plain, gray (diagonally) shaded and red (horizontally) shaded histograms show $\text{SFR}_{\text{IR+UV}}/\text{SFR}_{\text{fit}}$ ($\text{SFR}_{\text{IR+UV}}/\text{SFR}_{1500}$ in the middle panel in (b)) values respectively for $10 < \text{SFR}_{\text{IR+UV}} [M_{\odot} \text{yr}^{-1}] < 100$, $\text{SFR}_{\text{IR+UV}} [M_{\odot} \text{yr}^{-1}] < 10$ and $\text{SFR}_{\text{IR+UV}} [M_{\odot} \text{yr}^{-1}] > 100$ samples. Units are $M_{\odot} \text{yr}^{-1}$.

of obscured AGNs and the stellar mass is shown in Daddi et al. (2007a).

However, we find that the trend in the $\text{SFR}_{\text{IR+UV}}/\text{SFR}_{\text{fit}}$ ratio extends also at lower star formation rates (with average values lower than unity) and at lower redshifts. It is therefore possible that it reflects a change in the intrinsic physical properties of star-forming galaxies. A possible explanation is related to metallicity effects. Galaxies with sub-solar metallicities have lower mid-IR emission (at least at $8\mu\text{m}$, Calzetti et al. 2007) and higher UV luminosity than solar ones, for a given level of SFR. The observed trend can therefore be due to a metallicity trend, which is natural to expect given the observed mass–metallicity relation from low to high redshifts (Maiolino et al. 2008, and references therein). Unfortunately, a direct check of the statement above is not feasible. Reliable metallicities can not be inferred from broad band SED fitting, and high resolution spectroscopy is necessary to properly distinguish between SEDs characterized by different lines and hence metallicities.

Alternatively, the observed trend can be taken as evidence for a failure of the assumption that a single attenuation law can adequately model the output from a star-forming galaxy.

4. Mass assembly and downsizing

We now discuss the star formation properties of our galaxy sample as a function of redshift and stellar mass.

With respect to other surveys, our sample has the distinctive advantage of being selected through a multi-wavelength approach. In this section we will use the subsample B. The K_s and $m_{4.5}$ cuts ensure a proper sampling of highly absorbed star-forming galaxies, and hence a likely complete census of all galaxies with large SFR. On the other hand, the deep z -selected sample collects the fainter and bluer galaxies with low levels of dust extinction and star formation rate.

On this catalog, we will derive the SFR using the $\text{SFR}_{\text{IR+UV}}$ estimates for all objects with $F_{24\mu\text{m}} \geq 20 \mu\text{Jy}$, and the SFR_{fit} for all the fainter objects, and we will refer to it as IR-based. We remind that the $\text{SFR}_{\text{IR+UV}}$ star formation rates are derived by the mid-IR emission, computed with the DH synthetic models, and adopting the lowering correction of Papovich et al. (2007) at large SFRs. This technique has been widely adopted in the recent literature, and we adopt it as baseline. At the same time, we will mention how the results would be changed by using SFR_{fit} for all the objects. We will use the stellar masses estimates resulting from the SED fitting analysis as described above.

Finally, to avoid to bias the IR-based SFR estimates, in the following we will remove the obscured AGN candidates (Fiore et al. 2008) from our analysis. We are aware that the re-

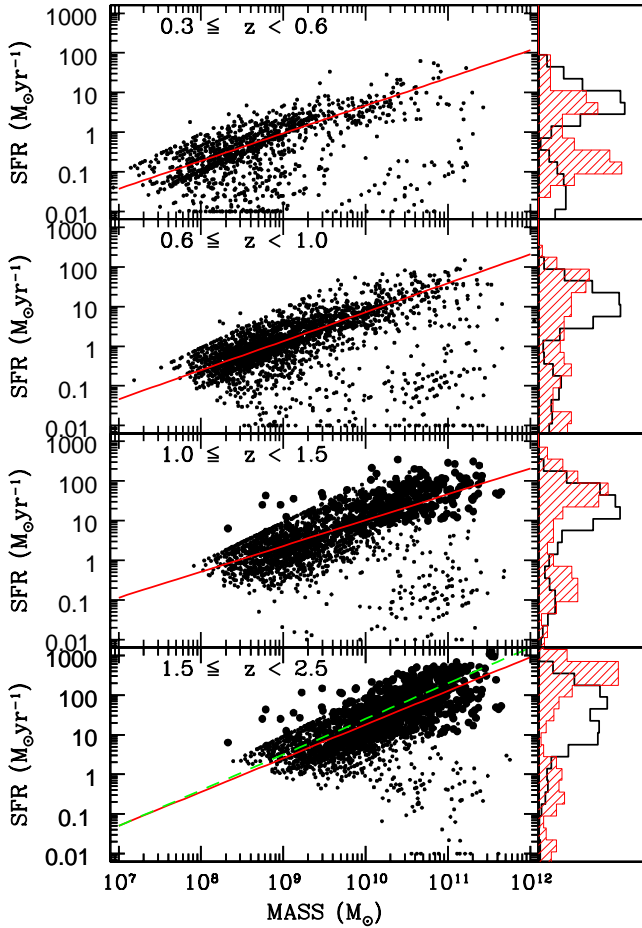


Fig. 4. Left panels: relation between the star formation rate and the stellar mass of the GOODS–MUSIC galaxies at different redshifts; large dots represent the galaxies with SFR derived from the $24\ \mu\text{m}$ emission, while small ones are $24\ \mu\text{m}$ undetected galaxies, with SFR derived from the SED fitting analysis; red solid lines show the 2σ -clipped least square fit described in the text; green dashed line in the highest redshift bin represents the correlation found by Daddi et al. (2007b). Right panels: SFR distribution in two mass bins, $10^{10} - 10^{11} M_{\odot}$ (plain black histograms) and $10^{11} - 10^{12} M_{\odot}$ (shaded red histograms).

removal of this population will cause a depletion of the star formation rate measured at high masses. Indeed, AGNs are known to reside preferentially in high mass sources (Best et al. 2005; Daddi et al. 2007a, Brusa et al., in prep.); although a high fraction of IR emission is thought to originate from accretion processes, some fraction of it likely derives from star formation.

4.1. The stellar mass–SFR relation

A direct relation between the stellar mass and the star formation rate in high redshift galaxies has been recently shown both at $z \approx 1$ (Elbaz et al. 2007) and in a subsample of star-forming BzK–SF at $z \approx 2$ (Daddi et al. 2007b). To some extent, this is at variance with the properties of galaxies in the local Universe, where the most massive galaxies have very low levels of star formation rate (Heavens et al. 2004). We present the global evolution of

this relation by plotting in Fig. 4 the star formation rate of each galaxy as a function of the corresponding stellar mass.

It is immediately clear that a trend between star formation rate and stellar mass is present at all redshifts. This relation is neither tight nor univocal, of course: at all redshifts, indeed, there exists a fraction of galaxies with low star formation rate, as also shown by the inset histograms. The SFR distribution gets more and more bimodal with decreasing redshifts. Fig. 4 also shows that at the highest redshifts only the most massive galaxies are already witnessing a quiescent phase.

We note that we are incomplete at low masses and SFRs because of the magnitude limit of the sample.

Nevertheless, there is a clear trend between SFR and M of the star-forming galaxies. To quantify it, we have computed a 2σ -clipped least square, assuming the relation $SFR = A(M/10^{11} M_{\odot})^{\beta}$. We find values for (A, β) equal to (23.33, 0.70), (38.91, 0.73), (46.18, 0.65), (128.03, 0.85), respectively in the four redshift bins from $z \sim 0.3$ to $z \sim 2.5$. The increase of the normalization A is robust, and it is due to the global increase of the star formation rate with redshift. The steepening of the slope, instead, is less robust, since it depends on the threshold used for the σ -clipping and on the SED fitting parameters, e.g. the minimum galaxy age. With a 3σ -clipping, slopes can vary by $\sim 20\%$. Considering these uncertainties, our results are in broad agreement with previous studies (Daddi et al. 2007b; Elbaz et al. 2007).

It is interesting to note that the correlation between SFR and stellar mass holds also using the SFR_{fit} estimates. While the two correlations are consistent at intermediate redshifts, the slope of the SFR_{fit} one is steeper at low redshift (0.90) and milder at high redshift (0.42), because of the systematic trends shown in Fig. 3.

4.2. The evolution of the cosmic star formation rate density

The most concise representation of the evolution of the star formation rate across cosmic time is the Star Formation Rate Density (SFRD), that we show in Fig. 5.

We show both the IR-derived estimates (continuous lines) as well as those obtained purely by the SED fit (dashed line). In this figure only, we extend the analysis to the redshift bin $2.5 < z < 3$. In this redshift regime, the IR templates are hardly representative, since the $24\ \mu\text{m}$ band is not representative of the dust emission peak anymore, although the Dale & Helou (2002) models are still formally applicable. For these reasons, the $SFR_{\text{IR+UV}}$ estimate is very tentative and should be looked at with caution.

Because of the complex selection criteria that we adopted, it is not easy to compute the corrections necessary to include the contribution of galaxies fainter than those included in our sample. Thanks to our mid-IR selection, we assume that we include nearly all highly star-forming galaxies. The missed fraction is therefore mainly made of galaxies with low star formation activity, sampled by the z -selection. A good approximation for our incompleteness can be obtained by fitting the star formation rate function computed on the z -selected sample in each redshift bin. Volumes have been computed with the $1/V_{\text{max}}$ method. We find that the SFR functions can be fitted with Schechter functions having slopes ~ -1.5 . We then correct our observations with the contributions extrapolated from the fitted functions at low SFR values. The corrections are small for $z < 2.5$, of the order of 10%, consistently with the assumption that the sample is complete at high star formation rate values. At $z > 2.5$ the corrections are higher than 50%.

We first note that the total SFRD (upper panel of Fig. 5) which we derive from our sample (black stars) nicely matches

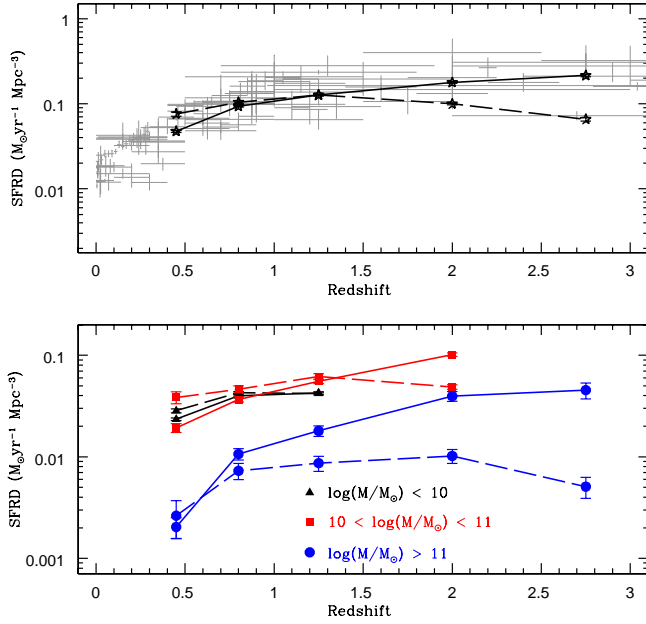


Fig. 5. Upper panel: the redshift evolution of the total cosmic SFRD. Solid lines refer to IR-based estimates, dashed lines to SED fitting estimates. The compilation of Hopkins & Beacom (2006) is shown as small gray dots. Lower panel: the redshift evolution of the cosmic SFRD by galaxies of different masses. Only galaxies above the completeness limit in stellar mass at each redshift (see last column of table 1) are shown. Solid lines refer to IR-based estimates, dashed lines to SED fitting estimates. Black, red and blue symbols correspond to different mass ranges as shown in the legend. Error bars include uncertainties on the SFR estimates and Poissonian errors.

the compilation of other surveys made by Hopkins & Beacom (2006), normalized to a standard Salpeter IMF, and it is also in agreement with Le Floch et al. (2005) Caputi et al. (2007) and Rodighiero et al. (in prep.).

It is more interesting to study the trend of the SFRD for galaxies of different stellar masses (lower panel of Fig. 5). Previous surveys, such as the Combo-17 (Zheng et al. 2007, that traced the evolution of the SFRD up to $z \simeq 1$) and the GDDS one (Juneau et al. 2005, that first presented the evolution of the SFRD in a K_s -selected sample up to $z \simeq 2$), have shown that the contribution to the SFRD by the more massive galaxies (typically those with $M > 10^{11} M_\odot$) is negligible at small redshift, and becomes much larger at $z \gg 1$, witnessing the major epoch of formation of the more massive galaxies. Our data confirm this picture, with an increase by a factor 20 from $z \simeq 0.5$ to $z \simeq 2$. The sharp decline at low z suggests that these structures must have formed their stars at earlier epochs. Keeping in mind the caveat above about the reliability of $\text{SFR}_{\text{IR+UV}}$ at $z > 2.5$, we note that the increase of the star formation rate density in $M > 10^{11} M_\odot$ galaxies appears to halt at $z > 2.5$. This is expected since, at these z , the number density of $M > 10^{11} M_\odot$ galaxies drops quickly (Fontana et al. 2006; Marchesini et al. 2008).

The evolution of the SFRD for galaxies of different stellar masses is one of the many evidences of *downsizing*. Indeed, the *downsizing* can be seen as an evolution of the slope of the SFRD as a function of redshift, which gets steeper as high mass galaxies are considered. This is due to the more rapid evolution of

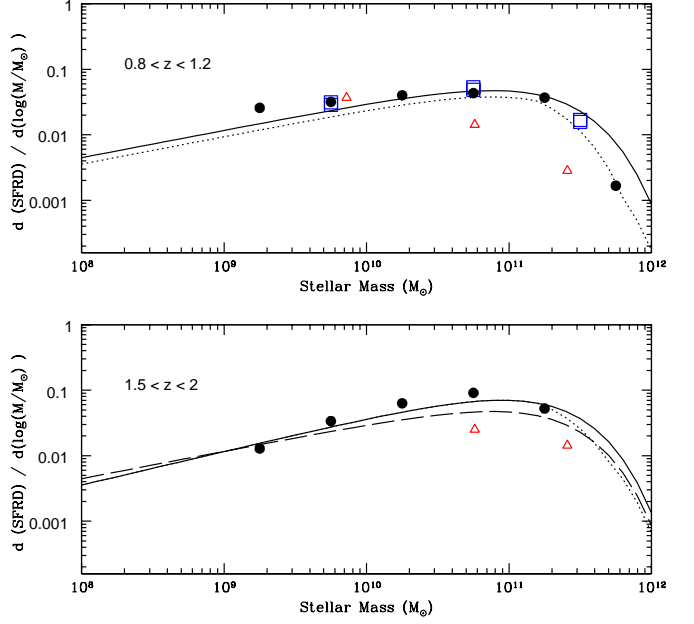


Fig. 6. The contribution to the cosmic SFRD by galaxies of given mass, in two redshift bins. Solid and dashed lines are computed assuming $f(M) = 1$. The dashed line in the lower panel correspond to the $z \simeq 1$ line of the upper panel. Dotted lines are computed assuming $f(M) \neq 1$ (see text). Black filled dots: this work; blue squares: Combo-17 (Zheng et al. 2007); red open triangles: GDDS (Juneau et al. 2005).

massive galaxies, where a number of physical processes are expected to suppress the star formation more efficiently than in lower mass galaxies.

The exact values of the SFRD depend very sensitively on the mass ranges adopted. Our mass bin choice is determined by the intention of having good statistics in each bin. Keeping in mind this warning, our observations seem to support the *downsizing* picture for the reasons mentioned above. Indeed, in the redshift interval $0.3 - 1.5$, where all mass samples are complete, the SFRD derived from the IR emission increases by a factor 1.8, 2.75 and 9 respectively for bins of increasing mass. We also recover a similar steepening of the slope of the relation between the average star formation rate per unit mass (which is treated in Sect. 4.3) and the redshift as moving from low to high mass galaxies.

In any case, at all observed redshifts the more massive galaxies do not dominate the global SFRD. To some extent, this may follow from the exact choice of the mass bins. However, it is easy to predict that the major contributors to the global SFRD are galaxies immediately below the characteristic mass M^* . The number of galaxies of given mass $N(M)$ at any redshift can be represented as a Schechter function ($N(M) \propto (M/M^*)^\alpha \exp(-M/M^*)$). Given the tight correlation between stellar mass and star formation rate described above ($\dot{M} \propto M^\beta$), and assuming that the fraction of star-forming galaxies is $f(M)$, the contribution to the cosmic SFRD for galaxies in a logarithmic interval $d\log M$ is simply

$$\frac{d(\text{SFRD}(M))}{d\log(M)} \propto (M/M^*)^{\alpha+\beta+1} \exp(-M/M^*) f(M) \quad (3)$$

Since α is in the range $\approx -1.2 / -1.4$ (Fontana et al. 2006) and $\beta \approx 0.6 - 0.9$ (see above, relating to the IR-based estimate), and ignoring for the moment $f(M)$, the shape of the $d(SFRD(M))/d\log(M)$ is that of a Schechter function with positive slope, which has a peak around M^* and decreases at $\log(M) < \log(M^*)$. The shape of $f(M)$ is somewhat more uncertain. We will simply assume that the fraction of active galaxies above the characteristic mass is around 0.5 at $z \approx 1$ and around 0.8 at $z \approx 2$ and that it will likely be larger at smaller masses (around 0.8 at $z \approx 1$ and around unity at $z \approx 2$). As a result, it will further decrease the distribution of $d(SFRD(M))/d\log(M)$ at large masses, without affecting the low mass regime.

Using the parameters of the Galaxy Mass Function obtained in Fontana et al. (2006), and the SFR–stellar mass correlation shown above, we have computed the expected $d(SFRD(M))/d\log(M)$ distribution in two redshift bins, 0.8–1.2 and 1.5–2, where the data from different surveys (Zheng et al. 2007; Juneau et al. 2005) can be combined. To convert masses and SFRs of Zheng et al. (2007) from a Chabrier (2003) to a Salpeter (1955) IMF we use a factor of 1.78 (Bundy et al. 2006) and 1.5 (Ferreiras et al. 2005) respectively. Masses and SFRs of Juneau et al. (2005) were instead renormalized from a Baldry & Glazebrook (2003) to a Salpeter (1955) IMF using the factors 1.82 (Juneau et al. 2005) and 2 (Hopkins & Beacom 2006).

Note that the argument presented above is not affected by the well known discrepancy between the directly measured mass density and the one inferred from the integration of the star formation rate density (Wilkins et al. 2008). The point here does not concern the integrated amount of stars formed, but only the analytical shape of the SFRD.

The result is shown in Fig. 6, where we plot the expected $d(SFRD(M))/d\log(M)$ distribution both assuming $f(M) = 1$ and a $f(M)$ which decreases for increasing masses and decreasing redshifts. Our data are well consistent with the ones provided by Zheng et al. (2007), who infer SFR estimates using the same method that we adopt to compute SFR_{IR+UV} . On the contrary, Juneau et al. (2005) estimate the SFR from the rest-frame UV continuum, and obtain lower values compared to SFR_{IR+UV} . The differences likely stem from the different selection criteria and SFR estimators used in their work.

This analysis confirms that the major contribution to the star formation derives from galaxies having masses around or immediately below the characteristic mass M^* . This statement is not inconsistent with the evolution of the SFRD for different mass bins that we show in Fig. 5. Indeed, the combination of the steepening of the SFR– M relation, the increase of the SFR values with increasing redshift, and the lower fraction of active galaxies at low z , prevails over the effect due to the decrease of the characteristic stellar mass at increasing z .

4.3. The specific star formation rate and the comparison with theoretical models

We plot in Fig. 7 the relation between the stellar mass and the specific star formation rate (SSFR hereafter) for all galaxies divided into redshift bins. To make the comparison between our findings and the Millennium Simulation predictions feasible, we convert our masses and SFR to the Chabrier (2003) IMF used by the Millennium Simulation.

We remind that our estimates of the SSFR are somewhat at the lower side of the possible estimates adopting standard values for SFR_{IR+UV} . On one side, the conversion between mid-IR flux and SFR includes a lowering factor for large SFRs, as de-

Δz	$\langle SSFR [Gyr^{-1}] \rangle$		
	IR+UV	SED fitting	$M_{lim} [M_\odot]$
0.3 - 0.6	0.275 ± 0.022	0.570 ± 0.137	$5 \cdot 10^9$
0.6 - 1.0	0.487 ± 0.017	0.654 ± 0.103	$8 \cdot 10^9$
1.0 - 1.5	0.755 ± 0.029	0.853 ± 0.168	$2 \cdot 10^{10}$
1.5 - 2.5	1.659 ± 0.058	0.424 ± 0.122	$7 \cdot 10^{10}$

Table 1. Average observed SSFR at different redshifts using IR- and fit-based estimates. Only galaxies above the completeness limit in stellar mass, shown in the last column of the table, have been considered. SSFRs and masses are calibrated to a Salpeter (1955) IMF.

scribed in Sect. 3.1 and in Appendix A. On the other side, using more recent models of stellar populations (Maraston 2005) would slightly decrease the average stellar masses (by 20% on average, see Salimbeni et al. 2009), and hence increase the derived SSFR.

First of all, we notice a strong bimodality in the SSFR distribution. Two distinct populations, together with some sources lying between the two, are detectable, one made up of young, active and blue galaxies (the so-called blue cloud) and the other one consisting of old, “red and dead”, early type galaxies (red sequence) (see also Fig. 4). The loci of these two populations are consistent with the selection in Salimbeni et al. (2008) between early and late type galaxies. It is noticeable how these evolved objects are already in place even at the highest redshift. We reserve a more complete discussion of these objects to Fontana et al. (2009).

A trend for the specific star formation rate to increase with redshift at a given stellar mass is evident: galaxies tend to form their stars more actively at higher redshifts. In fact, the bulk of active sources shifts to higher values of SSFR with increasing redshift. Our findings are in good agreement with Pérez-González et al. (2005) and Papovich et al. (2006).

A significant fraction of the sample, increasing with redshift, is in an active phase. It is natural to compare the SSFR (which has the units of the inverse of a timescale) with the inverse of the age of the Universe at the corresponding redshift $t_U(z)$. We will define galaxies with $M/SFR < t_U(z)$ as “active” in the following, since they are experiencing a major episode of star formation, potentially building up a substantial fraction of their stellar mass in this episode³. Galaxies selected following this criterium are forming stars more actively compared to their past history.

At $1.5 \leq z < 2.5$, the fraction of active galaxies in the total sample is 65%, and their mean SFR is $307 M_\odot yr^{-1}$. In order to compute the total stellar mass produced within this redshift interval, it would be necessary to know the duration of the active phase. At this purpose, we use a duty cycle argument and suppose that the active fraction of galaxies is indicative of the time interval spent in an active phase. We adopt the assumption that the active fraction is stable within the redshift bin considered. The time spanned in the 1.5–2.5 redshift interval corresponds to 1.5 Gyr. By multiplying the fraction of active galaxies by the time available, we derived an average duration of the active phase of 0.98 Gyr. The average amount of stellar mass assembled within each galaxy during these bursts is obtained as the product of the average SFR by the average

³ Indeed, if $M = \langle SFR \rangle_{past} \times t_U(z)$, where $\langle SFR \rangle_{past}$ is the star formation rate averaged over the whole age of the Universe at the corresponding z , the requirement $SFR/M > (t_U(z))^{-1}$ implies $SFR > \langle SFR \rangle_{past}$.

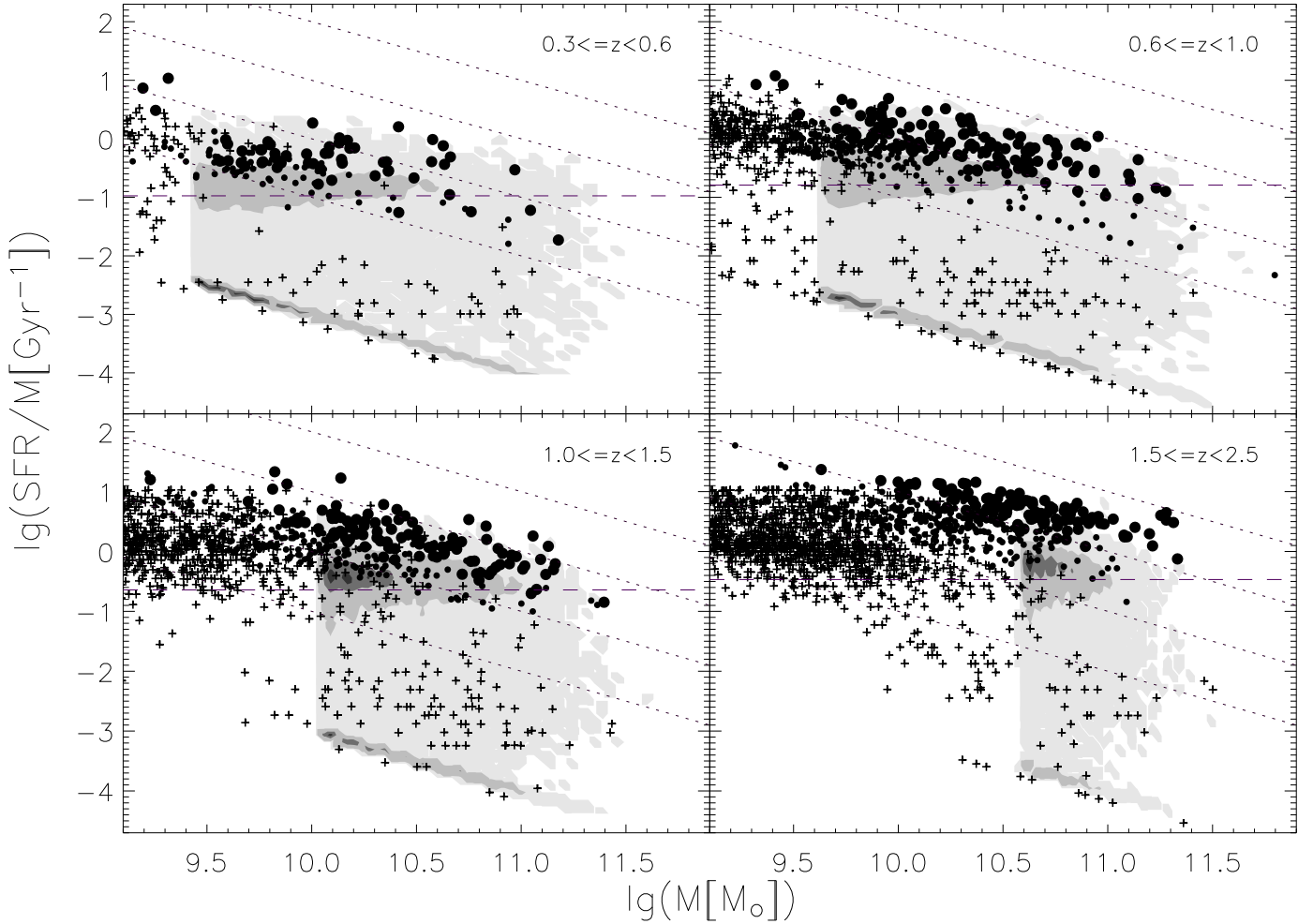


Fig. 7. Relation between the specific star formation rate and the stellar mass calibrated to a Chabrier (2003) IMF. Larger dots correspond to $24\ \mu\text{m}$ sources with $F_{24\mu\text{m}} > 83\ \mu\text{Jy}$, while smaller ones show $24\ \mu\text{m}$ detections with $20\ \mu\text{Jy} < F_{24\mu\text{m}} \leq 83\ \mu\text{Jy}$. Plus refer to $24\ \mu\text{m}$ upper limits. Dotted lines correspond to constant SFRs of 1, 10, 100 and $1000\ M_{\odot}\text{yr}^{-1}$. The horizontal dashed lines indicate the inverse of the age of the Universe at the center of each redshift interval. Shaded contour levels (at 0.05%, 10%, 50% and 80% level) represent the predictions of the Kitzbichler & White (2007) rendition of the Millennium Simulation.

duration of the active phase, and it is equal to $3.0 \times 10^{11} M_{\odot}$, which represents a significant fraction of the final stellar mass of the galaxies considered. Although quite simplified, this analysis implies that most of the stellar mass of massive galaxies is assembled during a long-lasting active phase at $1.5 \leq z < 2.5$. It is important to remark that this process of intense star formation occurs directly within already massive galaxies, and, given its intensity, prevails over growth due to merging events of already formed progenitors. A similar point is also stated by Daddi et al. (2007b). Independent arguments converging on the same result are based on the tightness of the SFR-mass relation (Noeske et al. 2007), on the kinematics of disks (Cresci et al. 2009) and on the analysis of the accretion histories of dark matter haloes in the Millennium Simulation (Genel et al. 2008).

To provide a further physical insight in this process, we have compared our results with the predictions of three recent theoretical models of galaxy formation and evolution. Our sample is affected by mass incompleteness, so only galaxies above the completeness limit in each redshift bin have been considered for the comparison. Note that such limit is dependent on the redshift bin. In Table 1 we report the average SSFR as a function of the

redshift bin for the IR- and the fit-based estimates, along with the mass cuts, computed as described in Fontana et al. (2006).

We show in Fig. 7 the predictions of a semi-analytical rendition of Kitzbichler & White (2007) of the Millennium N-body dark matter Simulation (Springel et al. 2005; Lemson & Springel 2006; De Lucia & Blaizot 2007), which adopts a WMAP1 cosmology. We find that the model grossly predicts an overall trend consistent with our findings. The SSFR decreases with stellar mass (at given redshift) and increases with redshift (at given stellar mass). In addition, it forecasts the existence of quiescent galaxies even at $z > 1.5$. However, the average observed SSFR is systematically under-predicted (at least above our mass limit) by a factor ~ 3 -5 by the Millennium Simulation. A similar trend for the Millennium Simulation at $z \sim 2$ was already shown by Daddi et al. (2007b).

We also compared our findings with the semi-analytical models of Menci et al. (2006) (adopting a cosmology consistent with WMAP1) and MORGANA (Monaco et al. 2007, updated by Lo Faro et al. subm., adopting a WMAP3 cosmology). They show very similar trends with respect to the Millennium Simulation, with only slightly different normalizations.

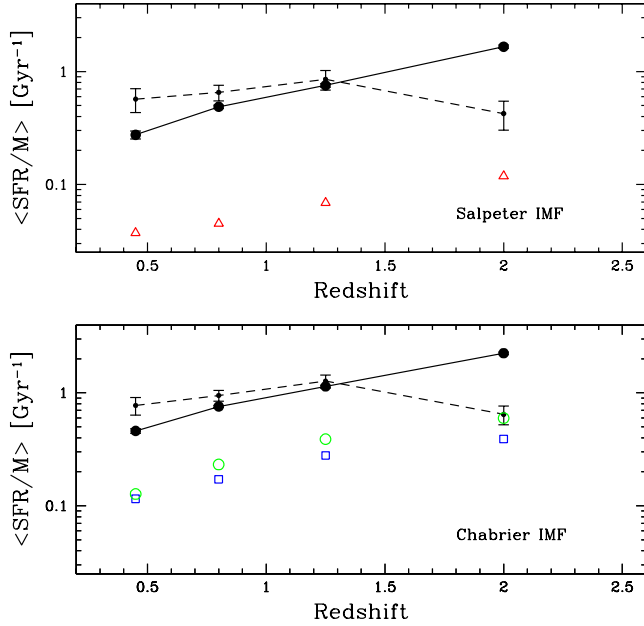


Fig. 8. Average SSFR in each redshift bin. Black solid lines refer to IR-based estimates, dashed lines to the SED fitting estimate. Error bars for the fit-based estimate are larger than those of the IR-based one because of the intrinsic parameter degeneracy involved with the SED fitting procedure. In the upper panel we show the comparison with Menci et al. (2006) semi-analytical model (red triangles), which adopts a Salpeter (1955) IMF. In the lower panel we compare our data with the predictions of the Millennium Simulation (Kitzbichler & White 2007) (blue squares) and MORFANA (green circles), which adopt a Chabrier (2003) IMF. The comparison is done above the completeness limit in stellar mass, which is different in each redshift bin (see text and table 1).

In Fig. 8 we plot the average SSFR as a function of the redshift bin for the IR- and the fit-based estimates as well as those predicted by the three theoretical models. Once again, we only consider galaxies above the completeness limit in mass in each redshift bin (see last column in table 1). The trend depicted must therefore be considered not an intrinsic trend, since we are observing different populations at the different redshifts because of the mass cuts. Errors on the average SSFR have been estimated through a Monte Carlo simulation.

We find that although all models taken into account reproduce the global observed trend, they predict an average star formation activity lower than the one observed in most of the mass regimes. The observed star formation occurring in situ in massive galaxies is larger than the one predicted by a factor 3–5 for the Millennium Simulation and for MORFANA, and around 10 for Menci et al. (2006) model. Daddi et al. (2007b) claims that the star formation rates predicted by the Millennium Simulation are up to one order of magnitude lower than the observed ones at $z \sim 2$. Similar mismatch at these redshifts between observed SFRs and those expected by various kind of theoretical models, independently on their physical processes implementations, have been found and discussed by Davé (2008). In order to reconcile data and model predictions, Khochfar & Silk (2008) suggest a possible scenario for the formation of galaxies at high redshift which is mainly driven by cold accretion flows. Their model al-

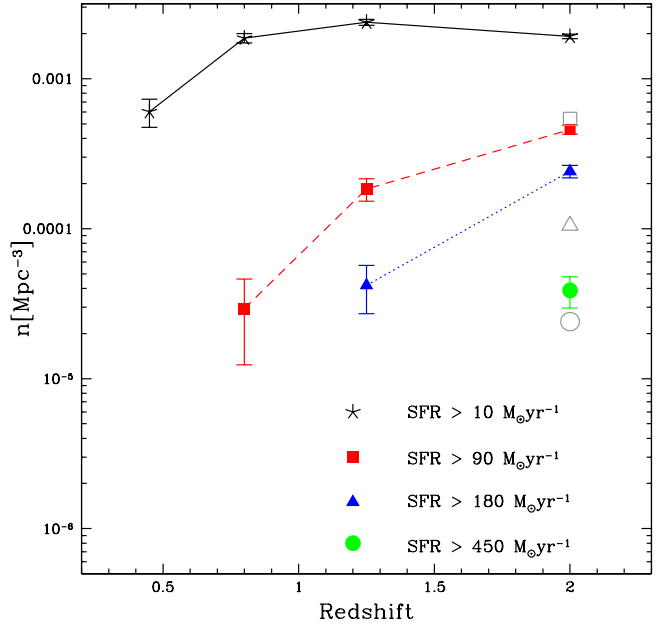


Fig. 9. Number density of star forming galaxies as a function of redshift and lower SFR. Filled symbols represent our observations corresponding to the SFR thresholds shown in the legend. Open gray symbols at $z \sim 2$ are the predictions of Khochfar & Silk (2008) model.

lows an increased star formation efficiency which results in a better agreement with observations.

We then considered the number density of galaxies having star formation rates higher than a fixed threshold as a function of redshift, and compared our observations with the model of Khochfar & Silk (2008) at $z \sim 2$. Fig. 9 shows our data (filled symbols) as well as theoretical predictions (open symbols). The SFR limits have been chosen in order to compare with Khochfar & Silk (2008) results⁴. The agreement is very good for objects with $SFR > 90 M_{\odot} \text{yr}^{-1}$, while the model slightly underpredicts the number density of galaxies with higher levels of star formation rate.

A most comprehensive comparison between theoretical predictions and observations can be found in Fontanot et al. (2009).

5. Summary and discussion

We have presented in this paper a revised version of our GOODS-MUSIC photometric catalog of the GOODS-S field. The major new feature of this release, on which the scientific discussion is based upon, is the inclusion of the $24 \mu\text{m}$ data taken from the Spitzer MIPS public images, of which we provide a self-consistent photometry for each object in the catalog. We employed a PSF-matching technique, performed by ConvPhot software (De Santis et al. 2007), to measure $24 \mu\text{m}$ photometry exploiting the high resolution z -ACS image used as a *prior* to detect the objects' positions. This allows to reduce effects of confusion noise and de-blending problems caused by the large dimensions of the MIPS PSF.

We have used this new catalog to study the star-forming properties of galaxies up $z \approx 2.5$.

⁴ Note that they adopt a Chabrier IMF, so the SFR thresholds have been renormalized adopting the conversion factors in Sect. 4.2.

We have first compared the estimates of the SFR obtained from the total IR luminosity ($\text{SFR}_{\text{IR+UV}}$) and from the SED fitting analysis to the overall 0.3 to 8 μm photometry (SFR_{fit}), which are the two major estimators of the SFR used so far in high redshift galaxies. We find that the two tracers are overall consistent, especially in the redshift range 0.3 – 1.5. The overall median ratio between $\text{SFR}_{\text{IR+UV}}$ and SFR_{fit} is around unity, with a limited number of objects severely discrepant. The agreement between the two estimators appears to depend on redshift, with a larger scatter at increasing redshifts, and a slight systematic overestimate of SFR_{fit} with respect to $\text{SFR}_{\text{IR+UV}}$ at the lowest redshift bin (0.3 – 0.6). The scatter increases significantly at $z > 1.5$, where the IR+UV value is systematically larger than the one resulting from the SED fitting analysis for bright objects. However, these results stem from a systematic trend that holds at all redshifts. Indeed, in galaxies with star formation rates $< 10 M_{\odot}/\text{yr}$ the fit-derived SFR is on average larger than $\text{SFR}_{\text{IR+UV}}$, while the opposite holds at $\text{SFR} > 100 M_{\odot}/\text{yr}$. It is at present difficult to ascertain the origin of this systematic trend. It can be due to systematics in interpreting the data, either arising in the SED fitting technique as the target galaxies move in redshift, or in the templates used in the extrapolation of the mid-IR observed flux, especially at high redshift, when it samples the PAH region. Alternatively, it could be due to physical origins, such as a metallicity trend or a failure of the assumption that a single attenuation law can adequately model the output from a star-forming galaxy.

Keeping in mind these uncertainties in the estimate of the star formation rate, we summarize here the basic results obtained adopting $\text{SFR}_{\text{IR+UV}}$, which we assume to be a more reliable tracer since it is not dust extincted.

- We show that, at all redshifts considered here, there is a correlation between the stellar mass and the star formation rate of star-forming galaxies. The logarithmic slope of this correlation, after applying a σ -clip to remove all quiescent galaxies, is in the range 0.6–0.9, with some indications of a steepening with increasing redshift.
- The SFRD derived from our sample agrees with the global trend already depicted by other surveys. When splitted according to stellar mass, it shows that more massive galaxies enter in their active phase at redshifts higher than lower mass ones. At $z > 2.5$, the increase in the SFRD due to the more massive galaxies (with $M > 10^{11} M_{\odot}$) appears to halt, in broad agreement with the expectations of theoretical models (Menci et al. 2004; Bower et al. 2006). This is mainly due to the fact that galaxies above such mass value become extremely rare at these redshifts. The increasing of the slope of the SFRD with redshift of samples of increasing mass seems to support the *downsizing* scenario.
- At all redshifts, the main contributors to the cosmic SFRD are galaxies around, or slightly below, the characteristic stellar mass M^* .
- Massive galaxies at $z \simeq 2$ are vigorously forming stars, typically at a rate of $300 M_{\odot}\text{yr}^{-1}$. A simple duty-cycle argument (see Sect. 4.3) suggests that they assemble a significant fraction of the final stellar mass during this phase.
- The specific star formation rate of our sample shows a well-defined bimodal distribution, with a clear separation between actively star-forming and passively evolving galaxies.

While these results are grossly independent on the particular star formation rate estimate, the specific details seem to depend on the chosen indicator. In particular, the correlation between the SFR and the stellar mass still holds using SFR_{fit} , but

it is steeper at $z \simeq 0.5$ and it gets flatter at high redshift, keeping very similar in the two intermediate redshift bins. As far as the star formation rate density and the specific star formation rate are concerned, the two techniques used to estimate the SFR give consistent results up to $z \sim 1.5$. However, significant differences arise at redshift $\gtrsim 1.5$, where the IR-based SFRD flattens and the fit-based one starts to decline. The average IR-based SSFR monotonically increases up to the highest observed redshifts, while the fit-based one has a turn-over around $z \sim 1.5$ and then decreases. The trends above directly reflect the correlation between $\text{SFR}_{\text{IR+UV}}$ and SFR_{fit} .

We use our results on the redshift evolution of the specific star formation rate, and its trend with the stellar mass, to investigate the predictions of a set of theoretical models of galaxy formation in Λ -CDM scenario.

On one side, these models reproduce the global trend that we find in the data – the most important being the increase of the specific star formation rate with redshift, and its trend with the stellar mass. Somewhat surprisingly, however, the average SSFR of galaxies in our sample is significantly larger than predicted by theoretical models, in most of the mass regimes. Essentially, after including a strict completeness limit in stellar mass, we find that the typical SSFR of galaxies of given mass is a factor at least $\simeq 3 - 5$ higher than predicted by the models we have included here. This mismatch is very clear for massive galaxies ($M_* \simeq 10^{11} M_{\odot}$) at $z \simeq 2$ and for less massive galaxies at $z \simeq 1$, where we have most of the statistics.

It is not obvious to ascertain the origin of this mismatch. On one hand, it could be due to a genuine failure of the models. Generically, such models tend to quench the star formation rate in massive galaxies to prevent the formation of blue, giant galaxies at low redshift, and to reproduce the existence of red, massive galaxies at high redshift. The mismatch that we observe could reveal that the feedback and star formation recipes adopted are too simplified or incorrect. Most of the models considered in this work adopt the commonly used star formation scenario, with gas uniformly collapsing towards the centre and forming a stable disk. New processes are now being explored (e.g. Dekel et al. 2009), which involve a more rapid formation of galaxies through cold streams and which could lead to a better agreement with observations.

Alternatively, the mismatch could be due to the overestimate of the stellar mass of the typical star-forming galaxy – for instance, due to a combination of the overestimate of merging events and of the star formation activity in its past history, i.e. at redshifts higher than those sampled in this work. A possible consequence of this can be noticed in the overestimate of the stellar mass function expected by the Millennium Simulation at high redshifts compared to the observations (Kitzbichler & White 2007).

Additional evidences for an incorrect treatment of the star formation processes derive from the recent works of Fontanot et al. (2009) and Lo Faro et al. (subm.). In the models they find an excess of low mass galaxies at $z < 2$ and faint LBGs at $z > 3$ respectively, which is likely balanced by the suppression of the star formation in order to reproduce the observed evolution of the SFRD.

However, we must remark that the interpretation of the observations is affected by a number of uncertainties, such as uncertainties on the stellar mass estimates or uncertainties originating both from the templates used to convert 24 μm fluxes into total infrared luminosities (see Appendix A) and in the SED fitting analysis. An example of these uncertainties is given by the mismatch between the integrated star formation rate density and

the stellar mass density. Such disagreement can be alleviated by an evolving IMF (Wilkins et al. 2008; Davé 2008), which would provide lower values for the SFR.

To make conclusive, quantitative statements in this direction it is ultimately needed to improve the reliability of the SFR measurements, especially for high redshift galaxies. Forthcoming IR facilities, such as Herschel and ALMA, will probably give us a more coherent picture.

Acknowledgements. We are grateful to Pierluigi Monaco, Niv Drory and Andrew Hopkins for the useful discussions. Observations were carried out with the Very Large Telescope at the ESO Paranal Observatory under Program IDs LP168.A-0485 and ID 170.A-0788 and the ESO Science Archive under Program IDs 64.O-0643, 66.A-0572, 68.A-0544, 164.O-0561, 163.N-0210, and 60.A-9120. The Millennium Simulation databases used in this paper and the web application providing online access to them were constructed as part of the activities of the German Astrophysical Virtual Observatory. This work has been partly funded by ASI, under the COFIS contract.

References

- Adelberger, K. L. & Steidel, C. C. 2000, *The Astrophysical Journal*, 544, 218
- Baldry, I. K. & Glazebrook, K. 2003, *ApJ*, 593, 258
- Bavouzet, N., Dole, H., Le Floc'h, E., et al. 2007, *ArXiv e-prints*, 712
- Bell, E. F. 2003, *ApJ*, 586, 794
- Bell, E. F., Papovich, C., Wolf, C., et al. 2005, *The Astrophysical Journal*, 625, 23
- Bell, E. F., Wolf, C., Meisenheimer, K., et al. 2004, *ApJ*, 608, 752
- Best, P. N., Kauffmann, G., Heckman, T. M., et al. 2005, *MNRAS*, 362, 25
- Bower, R. G., Benson, A. J., Malbon, R., et al. 2006, *MNRAS*, 370, 645
- Brinchmann, J. & Ellis, R. S. 2000, *ApJ*, 536, L77
- Brown, M. J. I., Dey, A., Jannuzi, B. T., et al. 2007, *ApJ*, 654, 858
- Bruzual, G. 2007a, *ArXiv Astrophysics e-prints*
- Bruzual, G. 2007b, in *Astronomical Society of the Pacific Conference Series*, Vol. 374, *From Stars to Galaxies: Building the Pieces to Build Up the Universe*, ed. A. Vallenari, R. Tantaló, L. Portinari, & A. Moretti, 303–+
- Bruzual, G. & Charlot, S. 2003, *Royal Astronomical Society, Monthly Notices*, 344, 1000
- Bundy, K., Ellis, R. S., Conselice, C. J., et al. 2006, *ApJ*, 651, 120
- Calzetti, D. 1997, *AJ*, 113, 162
- Calzetti, D. 2001, *PASP*, 113, 1449
- Calzetti, D. 2008, in *Astronomical Society of the Pacific Conference Series*, Vol. 390, *Astronomical Society of the Pacific Conference Series*, ed. J. H. Knapen, T. J. Mahoney, & A. Vazdekis, 121–+
- Calzetti, D., Armus, L., Bohlin, R. C., et al. 2000, *ApJ*, 533, 682
- Calzetti, D., Kennicutt, R. C., Engelbracht, C. W., et al. 2007, *ApJ*, 666, 870
- Calzetti, D., Kinney, A. L., & Storchi-Bergmann, T. 1994, *ApJ*, 429, 582
- Caputi, K. I., Lagache, G., Yan, L., et al. 2007, *ApJ*, 660, 97
- Chabrier, G. 2003, *ApJ*, 586, L133
- Chary, R. & Elbaz, D. 2001, *The Astrophysical Journal*, 556, 562
- Chary, R. R. 2006, *arXiv:astro-ph/0612736*
- Cimatti, A., Cassata, P., Pozzetti, L., et al. 2008, *A&A*, 482, 21
- Cowie, L. L., Songaila, A., Hu, E. M., & Cohen, J. G. 1996, *AJ*, 112, 839
- Cresci, G., Hicks, E. K. S., Genzel, R., et al. 2009, *ArXiv e-prints* 0902.4701
- Croton, D. J., Springel, V., White, S. D. M., et al. 2006, *MNRAS*, 367, 864
- Daddi, E., Alexander, D. M., Dickinson, M., et al. 2007a, *ApJ*, 670, 173
- Daddi, E., Cimatti, A., Renzini, A., et al. 2004, *ApJ*, 617, 746
- Daddi, E., Dickinson, M., Morrison, G., et al. 2007b, *ApJ*, 670, 156
- Dale, D. A. & Helou, G. 2002, *The Astrophysical Journal*, 576, 159
- Damen, M., Labbé, I., Franx, M., et al. 2009, *ApJ*, 690, 937
- Davé, R. 2008, *MNRAS*, 385, 147
- De Lucia, G. & Blaizot, J. 2007, *Royal Astronomical Society, Monthly Notices*, 375, 2
- De Santis, C., Grazian, A., Fontana, A., & Santini, P. 2007, *New Astronomy*, 12, 271
- Dekel, A. & Birnboim, Y. 2006, *MNRAS*, 368, 2
- Dekel, A., Birnboim, Y., Engel, G., et al. 2009, *Nature*, 457, 451
- Dey, A., Soifer, B. T., Desai, V., et al. 2008, *ApJ*, 677, 943
- Dickinson, M., Papovich, C., Ferguson, H. C., & Budavári, T. 2003, *ApJ*, 587, 25
- Drory, N., Bender, R., Feulner, G., et al. 2004, *The Astrophysical Journal*, 608, 742
- Dunne, L., Ivison, R. J., Maddox, S., et al. 2009, *MNRAS*, 394, 3
- Elbaz, D., Cesarsky, C. J., Chantal, P., et al. 2002, *Astronomy & Astrophysics*, 384, 848
- Elbaz, D., Daddi, E., Le Borgne, D., et al. 2007, *A&A*, 468, 33
- Faber, S. M., Willmer, C. N. A., Wolf, C., et al. 2007, *ApJ*, 665, 265
- Ferreras, I., Saha, P., & Williams, L. L. R. 2005, *ApJ*, 623, L5
- Feulner, G., Gabasch, A., Salvato, M., et al. 2005, *ApJ*, 633, L9
- Fiore, F., Grazian, A., Santini, P., et al. 2008, *ApJ*, 672, 94
- Fontana, A., Donnarumma, I., Vanzella, E., et al. 2003, *The Astrophysical Journal Letters*, 594, L9
- Fontana, A., Pozzetti, L., Donnarumma, I., et al. 2004, *Astronomy & Astrophysics*, 424, 23
- Fontana, A., Salimbeni, S., Grazian, A., et al. 2006, *Astronomy & Astrophysics*, 459, 745
- Fontana, A., Santini, P., Grazian, A., et al. 2009, *Accepted for publication in A&A*
- Fontanot, F., De Lucia, G., Monaco, P., Somerville, R. S., & Santini, P. 2009, *ArXiv e-prints* 0901.1130
- Genel, S., Genzel, R., Bouché, N., et al. 2008, *ApJ*, 688, 789
- Giallisco, M., Ferguson, H. C., Koekemoer, A. M., et al. 2004, *ApJ*, 600, L93
- Glazebrook, K., Abraham, R. G., McCarthy, P. J., et al. 2004, *Nature*, 430, 181
- Grazian, A., Fontana, A., De Santis, C., et al. 2006, *Astronomy & Astrophysics*, 449, 951
- Grazian, A., Salimbeni, S., Pentericci, L., et al. 2007, *Astronomy & Astrophysics*, 465, 393
- Han, Z., Podsiadlowski, P., & Lynas-Gray, A. E. 2007, *MNRAS*, 380, 1098
- Heavens, A., Panter, B., Jimenez, R., & Dunlop, J. 2004, *Nature*, 428, 625
- Hopkins, A. M. 2004, *The Astrophysical Journal*, 615, 209
- Hopkins, A. M. & Beacom, J. F. 2006, *ApJ*, 651, 142
- Iglesias-Páramo, J., Buat, V., Takeuchi, T. T., et al. 2006, *ApJS*, 164, 38
- Johansson, P. H., Naab, T., & Ostriker, J. P. 2009, *ArXiv e-prints* 0903.2840
- Juneau, S., Glazebrook, K., Crampton, D., et al. 2005, *ApJ*, 619, L135
- Kennicutt, Jr., R. C. 1998, *Annu. Rev. Astron. Astrophys.*, 36, 189
- Khochfar, S. & Ostriker, J. P. 2008, *ApJ*, 680, 54
- Khochfar, S. & Silk, J. 2008, *ArXiv e-prints* 0812.1183
- Kitzbichler, M. G. & White, S. D. M. 2007, *Royal Astronomical Society, Monthly Notices*, 376, 2
- Lagache, G., Dole, H., & Puget, J.-L. 2003, *Royal Astronomical Society, Monthly Notices*, 338, 555
- Le Floc'h, E., Papovich, C., Dole, H., et al. 2005, *ApJ*, 632, 169
- Lemson, G. & Springel, V. 2006, in *Astronomical Society of the Pacific Conference Series*, Vol. 351, *Astronomical Data Analysis Software and Systems XV*, ed. C. Gabriel, C. Arviset, D. Ponz, & S. Enrique, 212–+
- Lilly, S. J., Le Fevre, O., Hammer, F., & Crampton, D. 1996, *The Astrophysical Journal Letters*, 460, L1+
- Madau, P., Ferguson, H. C., Dickinson, M. E., et al. 1996, *Royal Astronomical Society, Monthly Notices*, 283, 1388
- Maiolino, R., Nagao, T., Grazian, A., et al. 2008, *A&A*, 488, 463
- Maraston, C. 2005, *MNRAS*, 362, 799
- Marchesini, D., van Dokkum, P. G., Forster Schreiber, N. M., et al. 2008, *ArXiv e-prints* 0811.1773
- Marcillac, D., Elbaz, D., Chary, R. R., et al. 2006, *Astronomy & Astrophysics*, 451, 57
- Menci, N., Cavaliere, A., Fontana, A., et al. 2004, *ApJ*, 604, 12
- Menci, N., Fontana, A., Giallongo, E., Grazian, A., & Salimbeni, S. 2006, *The Astrophysical Journal*, 647, 753
- Monaco, P., Fontanot, F., & Taffoni, G. 2007, *MNRAS*, 375, 1189
- Nagamine, K., Ostriker, J. P., Fukugita, M., & Cen, R. 2006, *ApJ*, 653, 881
- Noeske, K. G., Weiner, B. J., Faber, S. M., et al. 2007, *ApJ*, 660, L43
- Papovich, C. & Bell, E. F. 2002, *The Astrophysical Journal Letters*, 579, L1
- Papovich, C., Dickinson, M., & Ferguson, H. C. 2001, *ApJ*, 559, 620
- Papovich, C., Dole, H., Egami, E., et al. 2004, *ApJS*, 154, 70
- Papovich, C., Moustakas, L. A., Dickinson, M., et al. 2006, *The Astrophysical Journal*, 640, 92
- Papovich, C., Rudnick, G., Le Floc'h, E., et al. 2007, *ApJ*, 668, 45
- Pérez-González, P. G., Rieke, G. H., Egami, E., et al. 2005, *The Astrophysical Journal*, 630, 82
- Polletta, M., Tajer, M., Maraschi, L., et al. 2007, *The Astrophysical Journal*, 663, 81
- Popesso, P., Dickinson, M., Nonino, M., et al. 2009, *A&A*, 494, 443
- Pozzetti, L., Bolzonella, M., Lamareille, F., et al. 2007, *A&A*, 474, 443
- Rieke, G. H., Alonso-Herrero, A., Weiner, B. J., et al. 2009, *ApJ*, 692, 556
- Rieke, G. H., Young, E. T., Engelbracht, C. W., et al. 2004, *The Astrophysical Journal Supplement Series*, 154, 25
- Rudnick, G., Labbé, I., Förster Schreiber, N. M., et al. 2006, *The Astrophysical Journal*, 650, 624
- Salimbeni, S., Fontana, A., Giallongo, E., et al. 2009, *ArXiv e-prints* 0901.3540
- Salimbeni, S., Giallongo, E., Menci, N., et al. 2008, *A&A*, 477, 763
- Salpeter, E. E. 1955, *ApJ*, 121, 161
- Shapley, A. E., Steidel, C. C., Adelberger, K. L., et al. 2001, *ApJ*, 562, 95
- Shapley, A. E., Steidel, C. C., Erb, D. K., et al. 2005, *ApJ*, 626, 698

- Shupe, D. L., Rowan-Robinson, M., Lonsdale, C. J., et al. 2008, *AJ*, 135, 1050
- Siebenmorgen, R. & Krügel, E. 2007, *Astronomy & Astrophysics*, 461, 445
- Springel, V., White, S. D. M., Jenkins, A., et al. 2005, *Nature*, 435, 629
- Steidel, C. C., Adelberger, K. L., Giavalisco, M., Dickinson, M., & Pettini, M. 1999, *The Astrophysical Journal*, 519, 1
- Takeuchi, T. T., Buat, V., Iglesias-Páramo, J., Boselli, A., & Burgarella, D. 2005, *Astronomy & Astrophysics*, 432, 423
- Thomas, D., Maraston, C., Bender, R., & Mendes de Oliveira, C. 2005, *ApJ*, 621, 673
- Vanzella, E., Cristiani, S., Dickinson, M., et al. 2008, *A&A*, 478, 83
- Wilkins, S. M., Trentham, N., & Hopkins, A. M. 2008, *MNRAS*, 385, 687
- Wuyts, S., Labbé, I., Schreiber, N. M. F., et al. 2008, *ApJ*, 682, 985
- Yan, H., Dickinson, M., Giavalisco, M., et al. 2006, *ApJ*, 651, 24
- Zheng, X. Z., Bell, E. F., Papovich, C., et al. 2007, *ApJ*, 661, L41
- Zhu, Y.-N., Wu, H., Cao, C., & Li, H.-N. 2008, *ApJ*, 686, 155
- Zucca, E., Ilbert, O., Bardelli, S., et al. 2006, *A&A*, 455, 879

Appendix A: The estimate of total infrared luminosity

We present here the details regarding the method used to convert mid-IR fluxes into total infrared luminosities and compare the results obtained from different template libraries.

Supposing that the IR emission is primarily due to dust heating caused by star formation, the SFR results proportional to the dust thermal emission of the galaxy. Kennicutt (1998) asserts that the total infrared luminosity L_{IR} emitted between 8 and 1000 μm is a good tracer of the SFR. At the redshift of our interest ($z \sim 0.3 - 2.5$), MIPS 24 μm band probes the rest-frame mid-IR emission, which has been demonstrated to correlate with L_{IR} (e.g., Chary & Elbaz 2001; Elbaz et al. 2002; Papovich & Bell 2002; Takeuchi et al. 2005; Zhu et al. 2008).

L_{IR} extrapolation from 24 μm observations is quite a delicate point as dust emits most of its light at longer wavelengths. Moreover, the rest-frame region under study is particularly complex given the presence of polycyclic aromatic hydrocarbon (PAH) lines. In principle, these aspects could easily lead to non negligible errors in the determination of L_{IR} values. Therefore, we employed two different methods to infer L_{IR} , examining and comparing both synthetic and empirical templates using our K_s -selected subsample (subsample A).

Firstly, according to what is usually done in literature, we considered Dale & Helou (2002) (DH hereafter) and Chary & Elbaz (2001) (CE hereafter) synthetic libraries. These models do not extend to sufficiently short wavelengths to fit the SED shape, i.e. they do not include the stellar contribution, and at $z \gtrsim 1$ MIPS 24 μm band solely can be fitted, the other bands moving out of the model range or being shifted to the region dominated by star light. Each model is associated with a given L_{IR} . In the case of CE library, each model is provided with its absolute normalization, and hence with a given total infrared luminosity. As for the DH library, we assigned a given L_{IR} to each template using the empirical relation in Marcillac et al. (2006) between L_{IR} and the predicted $f_{\nu}^{60}/f_{\nu}^{100}$ colour. In both cases, for each source, once applied the k -correction, we selected the model which best reproduces the 24 μm observed luminosity and normalized it using the flux difference between the model and the observed galaxy.

In Fig. A.1 we show a comparison between L_{IR} as predicted by the two different model libraries. As already noticed in literature (Papovich et al. 2006; Marcillac et al. 2006), they give consistent results within a factor 2-3, with the highest differences appearing at high redshifts and high luminosities. Yet, it is possible to observe a few trends with both luminosity and redshift which depend on the specific templates details.

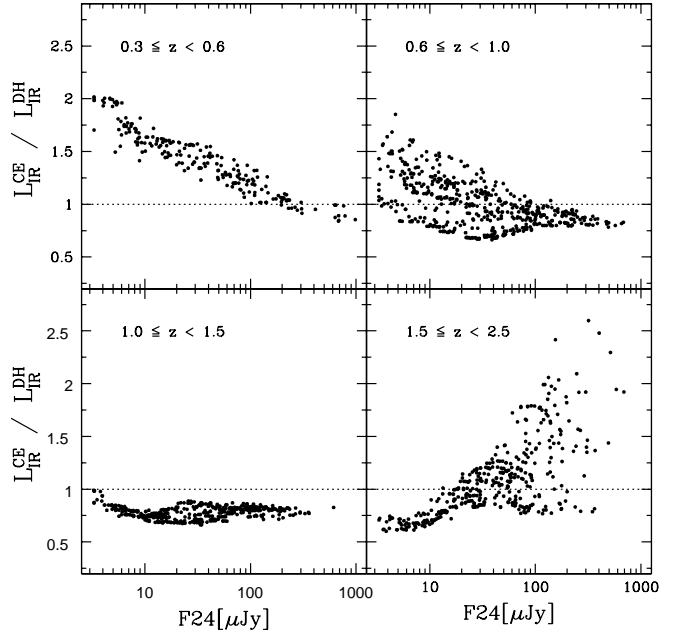


Fig. A.1. Comparison between the total infrared luminosity estimated with Dale & Helou (2002) and Chary & Elbaz (2001) templates in different redshift bins. The two synthetic libraries predictions are in good agreement within a factor < 3 .

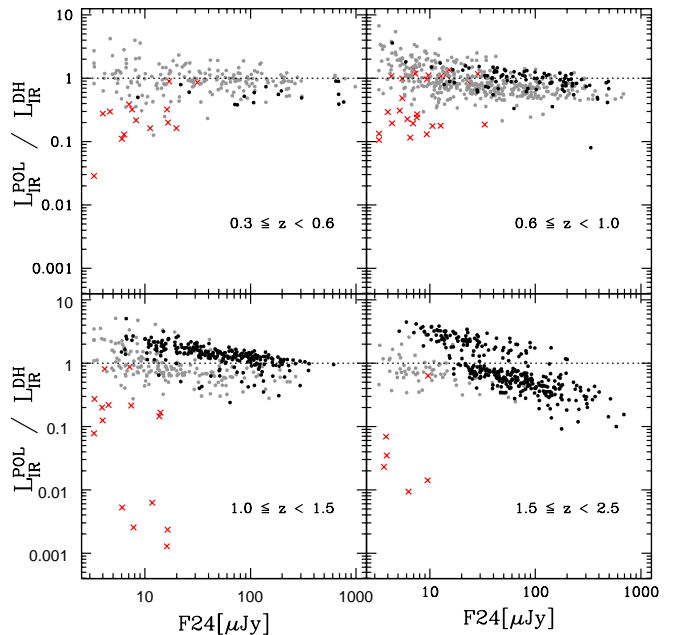


Fig. A.3. Comparison between the total infrared luminosity estimated with Dale & Helou (2002) and Polletta et al. (2007) templates. Black and gray dots and red crosses indicate objects fitted respectively by starburst, spiral-like and early-type templates by Polletta et al. (2007). Synthetic models appear to overestimate L_{IR} at bright luminosities in the highest redshift bin when compared to empirical templates.

A new kind of approach in our work consists in employing empirical local spectra to fit the overall galaxy SED shape in-

stead of the $24\ \mu\text{m}$ luminosity. Indeed, these spectra do include the stellar contribution as well as dust emission. We considered Polletta et al. (2007) spectra (POL hereafter). This library comprises early type, spiral, starburst and different kinds of AGN local templates, ranging from $\sim 100\ \text{\AA}$ to $\sim 5\ \text{mm}$. The wide wavelength extension allows us to fit the SED shape using the multi-band catalog. After performing several tests, we decided to carry out a fit over 5 bands (IRAC bands + $24\ \mu\text{m}$), in order to exclude the optical range, where the evolution of the stellar component dominates over the dust emission. Since we removed AGN-dominated objects from our sample, we only fit early type and star-forming models. If we instead include AGN SEDs, estimated L_{IR} are only poorly affected, resulting in slightly lower values (see also Papovich et al. 2007). Despite the poor statistical weight (one amongst five bands) and the larger noise, the $24\ \mu\text{m}$ band is still fitted acceptably. The mean deviation between observed and fitted magnitudes for $24\ \mu\text{m}$ detections is (-0.27 ± 0.74) mag, with 76% of objects consistent within 1σ , 82% of objects consistent within 2σ and 85% within 3σ (considering the $F_{24} > 20\ \mu\text{Jy}$ subsample). An example of different kinds of spectral energy distributions fitted by Polletta et al. (2007) templates is reported in Fig. A.2.

Figure A.3 shows the comparison between L_{IR} estimates obtained with DH synthetic library and POL empirical one. Sources classification based on the spectral shape fitting agrees with what presumed from $24\ \mu\text{m}$ emission. As expected, the only galaxies fitted by early type SEDs (red crosses) have very faint $24\ \mu\text{m}$ emission. Moreover, objects tend to be fitted by starburst-like models (black dots) rather than spiral-like ones (gray dots) as redshift increases. Although the scatter between the two estimates L_{IR} is larger than in the previous case (note that, contrarily to Fig. A.1, the y-scale is logarithmic), we find global consistency between the two adopted procedures. The only relevant deviation affects the highest redshift bin: in this redshift range synthetic models appear to over-predict, by up to a factor 10, L_{IR} for bright objects. The same behaviour has been observed in Papovich et al. (2007), where $24\ \mu\text{m}$ flux, fitted with DH library, seems to overestimate the SFR (which is fairly proportional to L_{IR}) with respect to the case where longer wavelengths (70 and $160\ \mu\text{m}$ MIPS bands) are considered as well. They correct this trend using an empirical second-order polynomial. A similar trend for the $24\ \mu\text{m}$ flux to overestimate L_{IR} at bright luminosities has also been pointed out in Bavouzet et al. (2007) and Rieke et al. (2009).

In our work we use Dale & Helou (2002) library for consistency with previous works and for which the lowering correction needed to estimate the SFR has been provided by Papovich et al. (2007).

We show L_{IR} , estimated using both synthetic (DH) and empirical (POL) templates, as a function of redshift in Fig. A.4. Once again, the two libraries give fairly consistent results. All in all, the conversion between fluxes and total infrared luminosity does not depend on the assumed templates in a significant way. The observed L_{IR} -redshift relation is in agreement with the one presented by Pérez-González et al. (2005). As expected, we are only able to detect the more luminous sources as we move to higher redshift.

Appendix B: Error analysis on SFR_{fit}

In Sect. 3.2 we have compared two different tracers for the star formation rate, one derived from the $24\ \mu\text{m}$ emission and the other inferred from a SED fitting technique. Although the two estimators have been found to be overall consistent, to a more

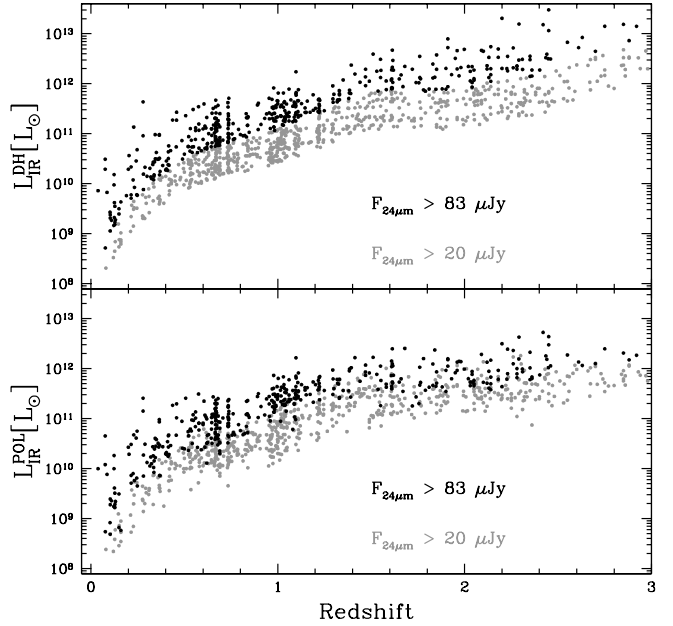


Fig. A.4. Relation between total infrared luminosity L_{IR} , computed using Dale & Helou (2002) (upper panel) and Polletta et al. (2007) templates (lower panel), and redshift. Black dots represent fluxes above $83\ \mu\text{Jy}$, gray + black dots refer to our sample limited at $20\ \mu\text{Jy}$.

attentive analysis they show a systematic trend depending on the SFR itself which is discussed in the text. In order to assess the reliability of the SFR measures inferred from the SED fitting, and hence of the concrete evidence of such characteristic trend, we make use of the error analysis which has already been widely adopted in similar cases (Papovich et al. 2001; Fontana et al. 2006, 2009). Briefly, the full synthetic library used to find the best fit spectrum is compared with the observed SED of each galaxy. For each spectral model (i.e. for each combination of the free parameters age , τ , Z , $E(B - V)$), the probability P of the resulting χ^2 is computed and retained, along with the associated SFR. In the case of galaxies with photometric z only, an additional source of error is the redshift uncertainty. To account for this, the error analysis has been done leaving the redshift free within the local minimum around z_{phot} .

We have chosen two subsamples for performing the error analysis, exemplifying respectively the cases $\text{SFR}_{\text{IR+UV}} \ll \text{SFR}_{\text{fit}}$ and $\text{SFR}_{\text{IR+UV}} \gg \text{SFR}_{\text{fit}}$. These two subsamples have been named subsample A and subsample B, and have been selected with the aim of having good statistics in both cases. Subsample A is made of galaxies having $0.6 \leq z < 1.0$, $\text{SFR}_{\text{IR+UV}} < 10 M_{\odot} \text{yr}^{-1}$ and $\text{SFR}_{\text{IR+UV}}/\text{SFR}_{\text{fit}} < 0.8$. Subsample B is composed of galaxies in the redshift bin $1.5 - 2.5$, with $\text{SFR}_{\text{IR+UV}} > 200 M_{\odot} \text{yr}^{-1}$ and $2 < \text{SFR}_{\text{IR+UV}}/\text{SFR}_{\text{fit}} < 20$. Highly obscured AGN candidates have been removed by both subsamples.

The results of our analysis are shown in Fig. B.1. We show the probability distribution of the star formation rates estimated through the SED fitting averaged over each subsample. We plot the probability associated to the SFR inferred from the generic fitted template, SFR_i , as a function of the ratio $\text{SFR}_i/\text{SFR}_{\text{best fit}}$. We also show the distribution and the average value of $\text{SFR}_{\text{IR+UV}}/\text{SFR}_{\text{best fit}}$.

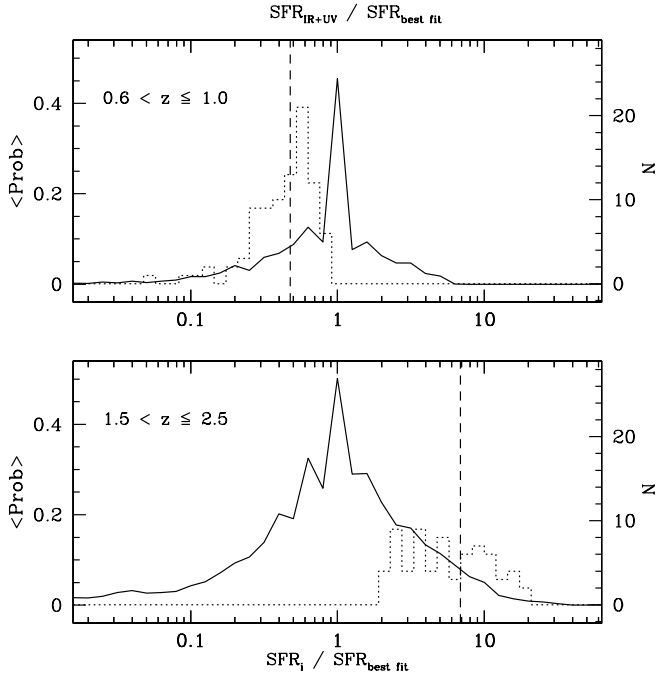


Fig. B.1. Probability distribution of the star formation rates estimated through the SED fitting technique averaged over each subsample. Upper and lower panels show respectively subsample A and B (see text). The solid line shows the probability associated to the SFR inferred from the generic fitted template, SFR_i , as a function of the ratio $\text{SFR}_i/\text{SFR}_{\text{best fit}}$. The dotted line shows the distribution of $\text{SFR}_{\text{IR+UV}}/\text{SFR}_{\text{best fit}}$ for all the galaxies in the subsample. The dashed line shows the average value for $\text{SFR}_{\text{IR+UV}}/\text{SFR}_{\text{best fit}}$.

As expected, the probability curve is much wider at higher redshifts than at lower z , where also the spread of our data gets larger (see Fig. 3). This is due to the faintness of the galaxies observed at these redshifts and to the larger k -corrections. However, it is clear from Fig. B.1 that the SED fitting for galaxies in both subsamples is well constrained, and that the inferred average SFR is significantly higher (lower) than the one derived from the IR emission. Indeed, the average $\text{SFR}_{\text{IR+UV}}/\text{SFR}_{\text{best fit}}$ (dashed line) as well as their distribution (dotted line), lies on the tail of the $\text{SFR}_i/\text{SFR}_{\text{best fit}}$ distribution.

We also inspected the individual probability curves, considering, for each source, the ratio between the probability of having SFR from the SED fitting equal to $\text{SFR}_{\text{IR+UV}}$ and the best fit probability $P(\text{SFR}_i = \text{SFR}_{\text{IR+UV}})/P(\text{SFR}_i = \text{SFR}_{\text{best fit}})$. The fraction of galaxies having this ratio greater than 0.4 is 5.6% and 18.8% in subsample A and B respectively.

Finally, according to a Kolmogorov Smirnov test, the probability that the SFR values derived from the two tracers are drawn from the same distribution is negligible ($1.4 \cdot 10^{-14}$ and $2.6 \cdot 10^{-20}$ respectively for subsample A and subsample B).

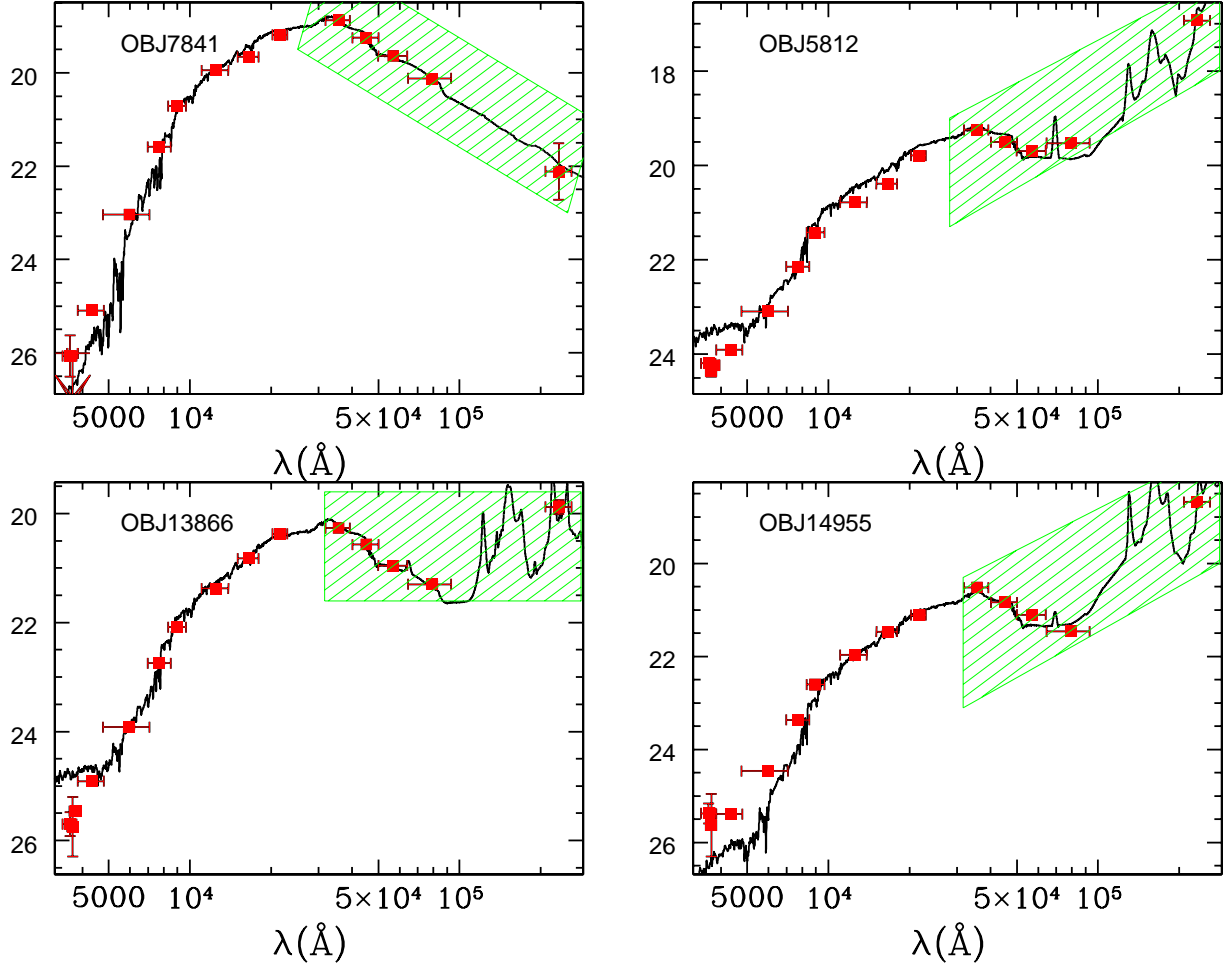


Fig. A.2. Different typical observed spectral energy distributions fitted by Polletta et al. (2007) templates. From top left, in anticlockwise direction, galaxies have been fitted by an elliptical, a spiral and two starbursts templates. The green shaded region indicates the wavelength range used for the fitting procedure.